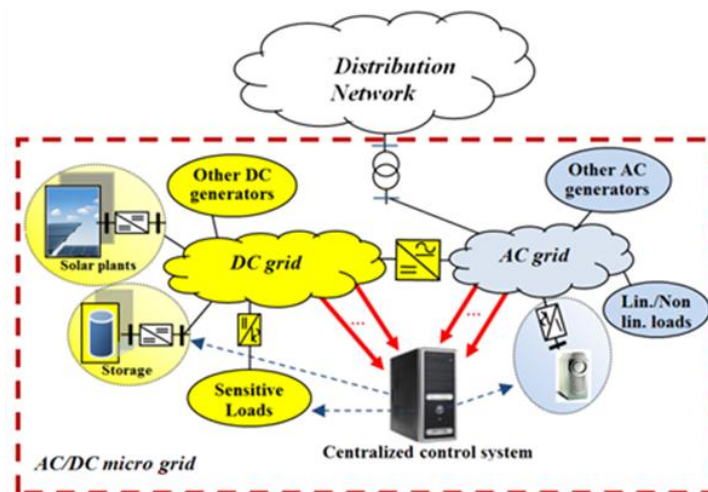


# Journal of Energy Challenges and Mechanics

ISSN 2056-9386

<http://www.nscj.co.uk/JECM/>

Volume 3, Issue 1  
February 2016



Featured article:

## On the comparison among optimal measurement placement methods for a hybrid micro grid harmonic state estimation. Part I: theoretical aspects

L. Alfieri<sup>1\*</sup>, A. Bracale<sup>2</sup>, P. De Falco<sup>1</sup>, M. Aprea<sup>1</sup>

<sup>1</sup>Department of Electrical Engineering and of Information Technology, University of Naples Federico II, Naples - 80125, Italy

<sup>2</sup>Department of Engineering, University of Naples Parthenope, Naples - 80143, Italy



North Sea Conference & Journal LTD  
2 Charlestown Walk, Cove Bay, AB12 3EZ, Aberdeen, Scotland, United Kingdom  
<http://www.nscj.co.uk/JECM/> | [jecm@nscj.co.uk](mailto:jecm@nscj.co.uk) | +44(0)1224 875635



TABLE OF CONTENTS

pages

<p><a href="#">Article 1</a>: On the comparison among optimal measurement placement methods for a hybrid micro grid harmonic state estimation. Part I: theoretical aspects <i>L. Alfieri<sup>1*</sup>, A. Bracale<sup>2</sup>, P. De Falco<sup>1</sup>, M. Aprea<sup>1</sup></i> <sup>1</sup><i>Department of Electrical Engineering and of Information Technology, University of Naples Federico II, Naples - 80125, Italy</i> <sup>2</sup><i>Department of Engineering, University of Naples Parthenope, Naples - 80143, Italy</i></p>	1-7
<p><a href="#">Article 2</a>: On the comparison among optimal measurement placement methods for a hybrid microgrid harmonic state estimation. Part II: numerical applications <i>L. Alfieri<sup>1*</sup>, A. Bracale<sup>2</sup></i> <sup>1</sup><i>Department of Electrical Engineering and of Information Technology, University of Naples Federico II, Naples - 80125, Italy</i> <sup>2</sup><i>Department of Engineering, University of Naples Parthenope, Naples - 80143, Italy</i></p>	8-14
<p><a href="#">Article 3</a>: Time varying waveform distortions caused by dispersed generators in Smart Grids <i>L. Alfieri<sup>1*</sup>, A. Bracale<sup>2</sup>, P. De Falco<sup>1</sup>, M. Aprea<sup>1</sup></i> <sup>1</sup><i>Department of Electrical Engineering and of Information Technology, University of Naples Federico II, Naples - 80125, Italy</i> <sup>2</sup><i>Department of Engineering, University of Naples Parthenope, Naples - 80143, Italy</i></p>	15-24
<p><a href="#">Article 4</a>: Hydrogenation of Carbon Dioxide to Synthetic Natural Gas: Impact of Catalyst Bed Arrangement <i>Andreas Martin<sup>*</sup>, Daniel Türks, Hesham Mena, Udo Armbruster</i> <i>Leibniz Institute for Catalysis, 18059 Rostock, Germany</i></p>	25-30
<p><a href="#">Article 5</a>: The Trend of ICT-based Renewable Energy in South Korea with a Focus on Cases of Application of Micro Grids <i>Suhyeon Han<sup>1*</sup>, Eunjin Jun<sup>1</sup>, Yuri Yoon<sup>1</sup>, Chulho Park<sup>1</sup></i> <sup>1</sup><i>Future Strategy Division, Green Technology Center, Seoul 100-705, South Korea</i></p>	31-35
<p><a href="#">Article 6</a>: Dynamics of surface photo-voltage in GaAs systems studied with time-resolved photoelectron spectroscopy <i>Masao Kamada<sup>1*</sup>, Junpei Azuma<sup>1</sup>, Senku Tanaka<sup>2</sup> and Kazutoshi Takahashi<sup>1</sup></i> <sup>1</sup><i>Synchrotron Light Application Center, Saga University, Saga 840-8502, Japan</i> <sup>2</sup><i>Department of Electric and Electronic Engineering, Faculty of Science and Engineering, Kinki University, Higashiosaka 577-8502, Japan</i></p>	36-41



# On the comparison among optimal measurement placement methods for a hybrid micro grid harmonic state estimation. Part I: theoretical aspects

## 关于混合微电网谐波状态估计的最佳测量选择方法之比较。第一部分：理论方面

L. Alfieri<sup>1\*</sup>, A. Bracale<sup>2</sup>, P. De Falco<sup>1</sup>, M. Aprea<sup>1</sup>

<sup>1</sup>Department of Electrical Engineering and of Information Technology, University of Naples Federico II, Naples - 80125, Italy

<sup>2</sup>Department of Engineering, University of Naples Parthenope, Naples - 80143, Italy

[luisa.alfieri@unina.it](mailto:luisa.alfieri@unina.it)

Accepted for publication on 12<sup>th</sup> October 2015

**Abstract** - The dynamic state estimation is an important issue in the management and control of micro grids ( $\mu$ Gs), since given the existence of distributed energy resources and time-varying, non-linear loads. In this paper, dynamic harmonic state estimation (DHSE) is used to evaluate the distortions of the voltage and current waveforms caused by the presence of time-varying, non-linear loads in hybrid AC/DC  $\mu$ Gs. A hybrid  $\mu$ G includes controllable and non-controllable loads, linear and non-linear loads, dispatchable and non-dispatchable dispersed generation units (such as a photovoltaic system and a gas micro-turbine) and energy storage systems. DHSE requires that voltage and current measurements be taken in correspondence with particular buses and lines of the system, which must be selected appropriately to guarantee that the system is observable. In this paper, we selected two techniques from the relevant literature for the optimal placement of the measurement units, and they were used for the DHSE with a Kalman filter (KF) on the hybrid AC/DC  $\mu$ G. The first method was based on the application of integer linear programming, and the second method was based on the minimum condition number of the measurement matrix. This paper reports the theoretical aspects of the methods that were used, and it is a companion paper to the Part II paper in which the results of the numerical experiments are presented.

**Keywords** - Optimal measurement placement, dynamic harmonic state estimation, Kalman filter, micro grid, power quality

### I. INTRODUCTION

To date, the structure and management of power distribution systems have been modified and improved

significantly due to the development of the new concepts of smart grids (SGs) and micro grids ( $\mu$ Gs). The increasing level of penetration of distributed generation, storage systems, and controllable loads is the main cause of these changes; the management of these new systems is guaranteed by the use of information and communication technologies [1-5]. In particular,  $\mu$ Gs can be classified as either AC or DC  $\mu$ Gs based on the supply voltage [2-4]. AC  $\mu$ Gs utilize the existing AC grid technologies, but DC  $\mu$ Gs can be used to connect the distributed generation sources that generate DC power. To gain the advantages of both types of grids, hybrid AC/DC  $\mu$ Gs have been proposed and developed recently, especially in industrial contexts in which dispatchable and renewable generation units, storage systems and controllable loads actively contribute to the operation of the electrical system [5]. The hybrid AC/DC  $\mu$ Gs are the main focus of this paper.

The optimal operation of hybrid  $\mu$ Gs requires careful consideration of both the technical and economic aspects of such systems, i.e., they must simultaneously satisfy increasing needs in terms of required power quality (PQ) and minimize costs. Optimal management usually is achieved by using a centralized control system (CCS) that operates based on estimates of the state of the system.

The estimates of the state of the system are used as input data for different tasks; for example, in [6], the estimates were used to compensate accurately for the harmonic disturbances, while, in [7], they were used for the real-time control of active and reactive power. In this paper, we dealt with the dynamic harmonic state estimation (DHSE) with the aim of estimating

the time-varying distortions of waveforms in the hybrid  $\mu$ G due to the presence of non-linear loads.

DHSE has been investigated extensively in the relevant literature, but the investigations have been focused mainly on AC networks [6, 8-14].

Specifically, in [8], a comprehensive review of the existing techniques was presented, specially focusing on neural network methods, which require long processing times. In [9, 10] the weighted least-squares estimator was used to minimize the error between the estimates and the measurements of the variables.

The Kalman filter (KF) was used in [6, 11, 12]. However, since the number of available measurements is usually smaller than the number of measurements required to determine the harmonic state of the network completely, the equation system that must be solved is usually underdetermined. Thus, it is essential to evaluate the observability of the system [13, 14].

It is well known that DHSE usually requires input data that consist of voltage and current measurements taken from opportunely selected buses and lines of the grid. The measurement units (MUs) fit for the purpose must fulfil specific requirements, especially in terms of sampling rates, synchronization of the measurements, and accuracy of the current and voltage transducers [15]. Phasor measurement units (PMUs), which have been studied extensively for high-voltage, AC transmission networks, seem to be among the most suitable devices for satisfying the aforesaid requisites. Their use in distribution networks is expected to increase significantly in the next few years due to the reductions of the manufacturing and installation costs that have resulted from technological improvements and the economies of scale [15, 16].

In the relevant literature, many techniques for the optimal allocation of MUs have been proposed for AC networks [17-26]. These techniques also can be used to collect the measurements required for the DHSE [27].

In [17-20], these techniques were classified on the basis of the algorithms that were used. The methods based on genetic algorithms are, substantially, adaptive heuristic research algorithms, that emulate natural evolution processes [21, 22]. These methods are very adaptive and robust, but they require long processing times; thus, they cannot be used when there are needs to reallocate MUs, which can arise when inevitable failures occur in obtaining measurements. In [23], particle swarm optimization was proposed for the placement of MUs. This method achieves the optimal placement of MUs, but it has the disadvantages of not accounting for the computational burden, not considering contingencies, and the lack of ease and versatility of implementation. In [24], an iterative procedure based on a binary search algorithm was proposed. This algorithm performs an exhaustive search by considering the possibility of faults in each line, but it is characterized by a heavy computational burden. In [25], a method was proposed based on the criteria of the minimum condition number of the measurement matrix. In [26], a fast, versatile technique was proposed based on integer linear programming (ILP); it solves

a binary, linear programming problem to guarantee the observability of the system.

In this paper, we propose to achieve DHSE on a hybrid AC/DC  $\mu$ G through a KF-based approach [6, 11, 28]. In this approach, time domain values of current and voltage measurements are required as inputs, and they are supplied by adequate MUs placed on the basis of the techniques proposed in [25, 26].

In the companion paper [29], numerical applications were performed on an AC/DC  $\mu$ G proposed for an actual industrial facility in southern Italy, and a comparison of the proposed approaches was developed on the basis of: (i) the number of measurements required to guarantee the observability of the system; (ii) the accuracy of the corresponding KF-based DHSE; and (iii) the computational burden.

This paper is organized as follows. Section II describes the architecture and the components of the hybrid  $\mu$ G that was considered. In Section III, the proposed optimal methods for the placement of the MUs are presented, and in Section IV the KF-based approach for the DHSE is presented. Our conclusions are reported in Section V.

## II. THE HYBRID AC/DC MICRO GRID UNDER STUDY

The general scheme of the hybrid AC/DC  $\mu$ G under study is shown in Fig. 1. The  $\mu$ G included linear and non-linear loads, dispatchable and non-dispatchable distributed generation units, and energy storage systems. A DC/AC static converter allowed the connection of the DC part of the  $\mu$ G (where non-dispatchable DC generators, sensitive loads, and energy storage systems are set) to the AC part of the  $\mu$ G (where dispatchable AC generators and linear/non-linear AC loads are set).

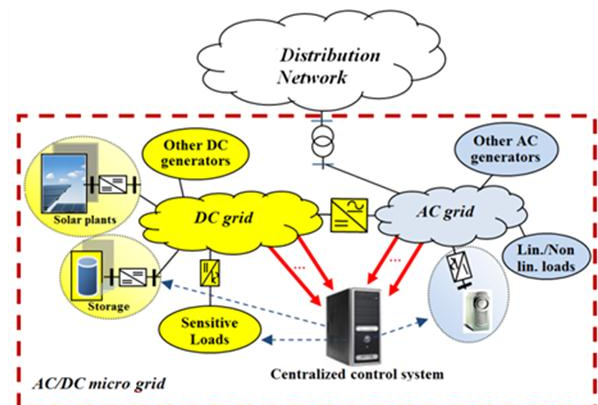


Fig. 1, The hybrid AC/DC  $\mu$ G general scheme.

Note that:

- sensitive AC loads are connected to the DC side of the  $\mu$ G through DC/AC static converters;
- DC generators are non-dispatchable photovoltaic systems that are connected to the DC grid through DC/DC static converters and equipped with a maximum power point tracker (MPPT) control system;

- the storage system is a battery that is connected to the DC grid through a DC/DC static converter;
- the AC generators, which are dispatchable generation units, are gas micro-turbines that are connected to the AC grid through AC/AC static converters.

The CCS in Fig. 1 performs the control strategy for the optimal operation of the entire system, and it operates on the basis of a dynamic estimation of the state of the system. The red arrows in Fig. 1 represent the measurements taken from the AC and DC sides of the  $\mu$ G. These measurements were selected on the basis of the optimal MUs placement techniques, reported in the following Section.

### III. PROPOSED OPTIMAL MUS PLACEMENT METHODS

In this paper, we used the *minimum condition number method (MCNM)* and the *integer linear programming method (ILPM)* proposed for AC networks in [25] and [26], respectively, in the case of the hybrid  $\mu$ G shown in Fig. 1. For the grid that we were considering, these methods were considered to be among the best procedures in terms of flexibility and computing time. We assumed that each MU was a multi-channel device that could measure the bus voltage in the bus in which it was installed and measure all of the line currents linked to that bus. Also, we assumed the MUs could fulfil the aforesaid requirements in terms of sampling rates, synchronization of the measurements, and the accuracies of the current and voltage transducers.

#### 3.1. MINIMUM CONDITION NUMBER METHOD

This method selects the minimum number of electrical variables that must be measured in order to guarantee the observability of the electrical system that is being assessed. It is based on the criterion of minimum condition number of the measurement matrix, which is obtained from the equation system that links the measurements to the unknown variables that must be estimated.

The condition number of a matrix is defined starting from the knowledge of the singular values of the matrix. In fact, considering a generic matrix  $T$  and indicating its conjugate transpose by  $T^*$ , the singular values of  $T$  are the square roots of the eigenvalues of the matrix  $T^*T$ . The condition number of a matrix is the ratio of the maximum singular value to the minimum singular value of the matrix.

In the phasor domain, for each harmonic order  $h$ , let  $\bar{Z}(h)$  be the measurements vector,  $\bar{X}(h)$  be the unknown vector of state variables to be estimated, and  $\bar{E}(h)$  be the measurement errors vector; it is possible to define the *measurement matrix*  $\hat{H}(h)$  from the mathematical model that links  $\bar{Z}(h)$  and  $\bar{X}(h)$  as follows:

$$\bar{Z}(h) = \hat{H}(h)\bar{X}(h) + \bar{E}(h) \quad (1)$$

Once  $\hat{H}(h)$  is determined, first an iterative procedure can be applied to determine the variables that must be measured, and, then, the number of MUs to be placed can be minimized through an exhaustive procedure.

It is well known that the measurement matrix  $\hat{H}(h)$  can be obtained from the relationships that link the bus voltages (which are the unknown variables to be estimated) to the load currents, line currents, or some other bus voltages (which can be measured).

If we let  $N$  be the number of buses, the relationship between the  $[N \times 1]$  complex vector  $\bar{I}_N(h)$  of load currents at each bus and the  $[N \times 1]$  complex vector  $\bar{V}_N(h)$  of bus voltages is given by:

$$\bar{I}_N(h) = \hat{Y}_{NN}(h)\bar{V}_N(h) \quad (2)$$

where  $\hat{Y}_{NN}(h)$  is the  $[N \times N]$  admittance matrix.

Obviously, the relationship between the complex vector  $\bar{V}_N(h)$  of bus voltages and itself is given by:

$$\bar{V}_N(h) = \mathbf{I}_{NN}\bar{V}_N(h) \quad (3)$$

where  $\mathbf{I}_{NN}$  is the  $[N \times N]$  identical matrix.

The relationship between the  $[L \times 1]$  complex vector  $\bar{I}_L(h)$  of the line currents and the complex vector  $\bar{V}_N(h)$  of the bus voltages is given by:

$$\bar{I}_L(h) = \hat{Y}_{LN}(h)\bar{V}_N(h) \quad (4)$$

where  $\hat{Y}_{LN}(h)$  is the  $[L \times N]$  line-bus admittance matrix.

In the most general case in which all load currents, all line currents, and all bus voltages can be measured, the measurement matrix  $\hat{H}(h)$  in eq. (1) is given by the combination of the matrices  $\hat{Y}_{NN}(h)$ ,  $\mathbf{I}_{NN}$ , and  $\hat{Y}_{LN}(h)$  in eqs. (2), (3), and (4), respectively; the size of matrix  $\hat{H}(h)$  is  $[M \times N]$ , where  $M = 2N + L$  is the maximum possible number of measurements.

An iterative procedure can be used to determine the minimum number of variables to be measured. Starting from the full-measurement matrix, at the first iteration, each possible measurement is excluded by eliminating the corresponding row in the matrix,  $\hat{H}(h)$ ; then, the different condition number is calculated for each reduced matrix, i.e.,  $\hat{H}_1(h), \hat{H}_2(h), \dots, \hat{H}_M(h)$ , obtained by respectively deleting row number  $1, 2, \dots, M$  from  $\hat{H}(h)$ . The matrix that presents the lower condition number (i.e.,  $\hat{H}_j(h)$ ) is chosen as the subject of the next iteration; each possible measurement is excluded by eliminating the corresponding row in the matrix  $\hat{H}_j(h)$ , the different condition number for each reduced matrix  $\hat{H}_{j_1}(h), \hat{H}_{j_2}(h), \dots, \hat{H}_{j_{M-1}}(h)$  is calculated, and the matrix that has the lowest condition number is chosen again as the subject of the next iteration. The whole iterative process is stopped when the size of the selected matrix is  $[N \times N]$ .

After the variables that are to be measured have been determined, we must determine the minimum number of MUs that must be installed in order to obtain those measurements in the most economical way possible. In order to minimize the number of MUs, the best choice is to employ multi-channel devices and to select their positions by a heuristic procedure, as described below:

1. when the measurement of a bus voltage or a load current is determined to be necessary in the above depicted iterative procedure, the corresponding bus is called the “major bus;” all other buses are called “minor buses,” and a MU is placed in all of the major buses;
2. if it is necessary to measure at least one of the line currents connected to a major bus, a channel of the MU placed in that major bus must be dedicated to measure that line current;
3. then, a MU is placed in the minor bus connected to the highest number of lines in which currents must be measured; this bus no longer can be considered to be suitable for the placement of a MU;
4. step 3 is repeated until none of the remaining minor buses is linked to a line in which current must be measured and is not yet measured by another MU.

In [25], the aforesaid approach was applied for each harmonic order of interest. In this paper, since the considered MUs acquire waveform samples in the time domain, the iteration of the aforesaid procedure at each harmonic order appeared to be redundant. Therefore, supported by the experimental applications reported in the companion paper [29], we propose to apply the procedure to the measurement matrix evaluated only for one appropriately-selected harmonic order.

### 3.2. INTEGER LINEAR PROGRAMMING METHOD

The method based on Integer Linear Programming is a fast, versatile technique based on the solution algorithm of a programming problem in which an objective function of integer variables is minimized under linear constraints. In [26], this method was proposed for the state estimation at the fundamental component, while, in this paper, it was used to get reliable state estimation for all of the harmonics considered in the hybrid  $\mu$ G shown in Fig.1.

The entire system is observable by allocating the right number of MUs in strategic buses. If there are  $N$  buses in the AC side of the  $\mu$ G, the problem of the optimal allocation of MUs can be solved by the formulation of an optimization problem in integer variables. The objective function to be minimized is:

$$f_{obj} = \sum_i^N w_i \cdot b_i \quad (5)$$

and the inequality constraints to be satisfied are:

$$\mathbf{f}(\mathbf{b}) \geq \hat{\mathbf{1}} \quad (6)$$

where:  $\mathbf{b} = \{b_1, b_2, \dots, b_N\}$  is a vector of decisional binary variables, with  $b_i = 1$  if a MU is placed in the  $i$ -th bus of the grid, otherwise  $b_i = 0$ ;  $w_i$  is a weight factor, which can be related to the cost of the single MU installed at the  $i$ -th bus;  $\hat{\mathbf{1}}$  is the unity vector;  $\mathbf{f}(\mathbf{b})$  is a vector function that is linked to the connectivity matrix of the system obtained from the non-oriented graph of the electrical circuit of the grid. The  $i$ -th component of this function expresses the observability of the  $i$ -th bus voltage: it is different from zero if, based on the interpretation of the graph through logical operators, at least one MU is placed in the  $i$ -th bus and/or in its nearby, linked buses.

The elements,  $S_{k,m}$ , of the binary connectivity matrix  $\mathbf{S}$  are defined as follows:

$$S_{k,m} = \begin{cases} 1 & \text{if } k = m \\ 1 & \text{if the } k^{\text{th}} \text{ and the } m^{\text{th}} \text{ buses are linked} \\ 0 & \text{otherwise} \end{cases} \quad (7)$$

The connectivity matrix  $\mathbf{S}$  can be identified directly by inspection of the electrical circuit or through the analysis of the bus admittance matrix by transforming its values in binary values. The vector function  $\mathbf{f}(\mathbf{b})$  is obtained as:

$$\mathbf{f}(\mathbf{b}) = \mathbf{S} \mathbf{b} \quad (8)$$

where  $f_i = S_{i1}b_1 + \dots + S_{iN}b_N$  is constrained to be not less than unity, i.e.,  $f_i \geq 1$ . Note that the operator “+” is intended as the logical operator “OR”, and the value “1” on the right of each inequality ensures that at least one of each variable that appears in the “sum” on the left is different from zero.

Note that the ILP method is based only on the inspection of the topology of the grid, so the results obtained from the optimal MUs placement are still valid even if these devices provide measurements in the time domain.

## IV. DYNAMIC HARMONIC SYSTEM STATE ESTIMATION

The DHSE procedure proposed in [6,11,28] for AC networks was applied to the case of the hybrid  $\mu$ G in Fig.1; this technique is based on the application of KF and considers the measurements provided by the MUs placed by applying both of the methods presented in Section III.

Since the only non-linear elements of a  $\mu$ G are the static converters, a linearized model of the system can be performed by modelling the non-linear load as harmonic current injection. In this way, the state-space model can be expressed through a matrix equation. Let  $\mathbf{x}$  be the state vector,  $\mathbf{u}$  be the controllable input vector,  $\mathbf{d}$  be the non-controllable input vector, and  $\mathbf{y}$  be the output vector. In particular, for the AC side of the  $\mu$ G,  $\mathbf{x}$  consists of the inductor currents and capacitor voltages,  $\mathbf{u}$  consists of the controllable current injections,  $\mathbf{d}$  consists of the disturbance currents, and  $\mathbf{y}$  consists of the busbar voltages. Then, the state-space model is:

$$\begin{cases} \dot{\mathbf{x}} = \mathbf{A}\mathbf{x} + \mathbf{B}\mathbf{u} + \mathbf{F}\mathbf{d} \\ \mathbf{y} = \mathbf{C}\mathbf{x} \end{cases} \quad (9)$$

where  $\mathbf{A}$ ,  $\mathbf{B}$ ,  $\mathbf{F}$ , and  $\mathbf{C}$  are matrices that can be obtained from the equivalent circuit of the  $\mu$ G.

In this paper, the disturbances  $\mathbf{d}$  in eq. (9) were modelled by harmonic current injections, caused by the non-linear loads of the grid [12]. By this model, the  $h$ -th current harmonic injected in the  $n$ -th bus can be expressed as follows:

$$d_{n,h}(t) = D_{n,h} \cos(\omega_h t + \varphi_{n,h}) \quad (10)$$

In order to express a dynamic disturbance model coherently with eq. (9), the following form can be stated for the  $h$ -th current harmonic:

$$\dot{\mathbf{z}}_{n,h} = \begin{bmatrix} \dot{d}_{n,h} \\ \dot{d}_{n,h} \end{bmatrix} = \begin{bmatrix} 0 & 1 \\ -\omega_h^2 & 0 \end{bmatrix} \cdot \begin{bmatrix} d_{n,h} \\ \dot{d}_{n,h} \end{bmatrix} = \mathbf{A}_{z_h} \mathbf{z}_{n,h} \quad (11)$$

where  $\mathbf{z}_{n,h}$  is the vector that includes the disturbance  $d_{n,h}$  in (10) and its first derivative  $\dot{d}_{n,h}$ .

Now, let  $\mathbf{h} = [d_{1,1}, \dots, d_{N,1}, \dots, d_{1,H}, \dots, d_{N,H}]$  be the vector of the harmonic disturbances,  $H$  be the number of the considered harmonics, and  $\mathbf{G}$  be the matrix defined as:

$$\mathbf{G} = \begin{bmatrix} -\omega_1^2 \mathbf{I}_N & \mathbf{0}_N & \dots & \mathbf{0}_N \\ \mathbf{0}_N & -\omega_2^2 \mathbf{I}_N & \dots & \mathbf{0}_N \\ \vdots & \vdots & \ddots & \vdots \\ \mathbf{0}_N & \mathbf{0}_N & \dots & -\omega_H^2 \mathbf{I}_N \end{bmatrix} \quad (12)$$

it results:

$$\dot{\mathbf{z}} = \begin{bmatrix} \dot{\mathbf{h}} \\ \dot{\mathbf{h}} \end{bmatrix} = \begin{bmatrix} \mathbf{0}_M & \mathbf{I}_M \\ \mathbf{G} & \mathbf{0}_M \end{bmatrix} \cdot \begin{bmatrix} \mathbf{h} \\ \dot{\mathbf{h}} \end{bmatrix} = \mathbf{A}_z \mathbf{z} \quad (13)$$

where  $\mathbf{0}_N$ ,  $\mathbf{0}_M$ ,  $\mathbf{I}_N$ , and  $\mathbf{I}_M$  are the null and identity square matrices of specified sizes, with  $M = H \cdot N$ .

Eqs. (9) and (13), disturbance component vector  $\mathbf{h}$ , and its derivative  $\dot{\mathbf{h}}$ , together with the state variables  $\mathbf{x}$ , form the expanded state variables  $\xi$  of the dynamic time-invariant system; therefore, it is:

$$\begin{bmatrix} \dot{\mathbf{x}} \\ \dot{\mathbf{z}} \end{bmatrix} = \begin{bmatrix} \mathbf{A} & \mathbf{F}_z \\ \mathbf{0} & \mathbf{A}_z \end{bmatrix} \cdot \begin{bmatrix} \mathbf{x} \\ \mathbf{z} \end{bmatrix} + \begin{bmatrix} \mathbf{B} \\ \mathbf{0} \end{bmatrix} \cdot \mathbf{u} \quad (14)$$

where  $\mathbf{F}_z$  is the matrix that relates the derivative state vector  $\dot{\mathbf{x}}$  to the vector  $\mathbf{z}$ , and it is constituted by  $H$  submatrices equal to the matrix  $\mathbf{F}$  and  $H$  null submatrices  $\mathbf{0}_F$  having the same size of  $\mathbf{F}$ , i.e., if  $H = 3$ ,  $\mathbf{F}_z = [\mathbf{F} \ \mathbf{F} \ \mathbf{F} \ \mathbf{0}_F \ \mathbf{0}_F \ \mathbf{0}_F]$ . Eq. (14) can be expressed in a more compact form as:

$$\dot{\xi} = \tilde{\mathbf{A}} \cdot \xi + \tilde{\mathbf{B}} \cdot \mathbf{u} \quad (15)$$

The relationship that links the expanded state variables  $\xi$  to measurement vector  $\zeta$  is:

$$\zeta = \tilde{\mathbf{C}} \cdot \xi \quad (16)$$

where  $\tilde{\mathbf{C}}$  is normally a sparse matrix in which the non-zero elements are unity and correspond to the variables of  $\xi$  that must be measured.

Now, let us assume that measurements are available for the dynamic state estimation at the generic time  $t_k = t_0 + kT_s$ , where  $T_s$  is the sample time; the model of the system described by eqs. (15) and (16) can be formulated in discrete-time form, as follows:

$$\begin{cases} \xi_k = \tilde{\mathbf{A}}_d \cdot \xi_{k-1} + \tilde{\mathbf{B}}_d \cdot \mathbf{u}_{k-1} + \mathbf{w}_{k-1} \\ \zeta_k = \tilde{\mathbf{C}} \cdot \xi_k + \mathbf{v}_{k-1} \end{cases} \quad (17)$$

where  $\xi_k = \xi(t = t_k)$ ,  $\tilde{\mathbf{A}}_d = \exp(\tilde{\mathbf{A}} T_s)$ , and  $\mathbf{w}_k, \mathbf{v}_k$  are process noise and measurement noise, usually assumed as independent, white noise, respectively, characterized by a Gaussian probability density function, and:

$$\tilde{\mathbf{B}}_d = \tilde{\mathbf{A}}^{-1} \cdot [\exp(\tilde{\mathbf{A}} T_s) - \mathbf{I}] \cdot \tilde{\mathbf{B}} \quad (18)$$

Starting from eq. (17), the recursive equations of KF can be expressed as:

- two *predictive time-update* equations:

$$\hat{\xi}_{k|k-1} = \tilde{\mathbf{A}}_d \cdot \hat{\xi}_{k-1|k-1} + \tilde{\mathbf{B}}_d \cdot \mathbf{u}_{k-1} \quad (19)$$

$$\mathbf{P}_{k|k-1} = \tilde{\mathbf{A}}_d \cdot \mathbf{P}_{k-1|k-1} \cdot \tilde{\mathbf{A}}_d^T + \mathbf{W} \quad (20)$$

- three *corrective measurement-update* equations:

$$\mathbf{K}_k = \mathbf{P}_{k|k-1} \cdot \tilde{\mathbf{C}}^T \cdot (\tilde{\mathbf{C}} \cdot \mathbf{P}_{k|k-1} \cdot \tilde{\mathbf{C}}^T + \mathbf{V})^{-1} \quad (21)$$

$$\hat{\xi}_{k|k} = \hat{\xi}_{k|k-1} + \mathbf{K}_k \cdot (\zeta_k - \tilde{\mathbf{C}} \cdot \hat{\xi}_{k|k-1}) \quad (22)$$

$$\mathbf{P}_{k|k} = (\mathbf{I} - \mathbf{K}_k \cdot \tilde{\mathbf{C}}) \cdot \mathbf{P}_{k|k-1} \quad (23)$$

where  $\mathbf{W}$  and  $\mathbf{V}$  are the process and measurement noise covariance matrices, respectively,  $\mathbf{K}_k$  is the *Kalman gain*,  $\mathbf{P}_{k|k}$  and  $\mathbf{P}_{k|k-1}$  are the covariance error matrix at time  $t_k$  and the prediction of the same matrix at time  $t_{k-1}$ , respectively, and  $\hat{\xi}_{k|k}$  and  $\hat{\xi}_{k|k-1}$  are the posterior and the prior estimation of the expanded state variables, respectively.

Note that the process noise covariance matrix  $\mathbf{W}$  also takes into account the model's uncertainties, thereby allowing the state estimation even if the knowledge of the grid parameters is not perfect. Therefore, this iterative algorithm provides an accurate monitoring of both disturbances and state variables.

## V. CONCLUSIONS

The state of a hybrid AC/DC  $\mu\text{G}$  must be known in order to perform optimal control of the system. However, economic issues make it unreasonable to monitor all of the state variables, so it is important to provide tools for the DHSE of the  $\mu\text{G}$  even when some of the desired measurements are not available.

According to this scenario, this paper provided of two methods for optimal placement of the MUs in hybrid AC/DC  $\mu\text{Gs}$ , both of which have been used previously in AC networks. Specifically, these two methods are the minimum condition number method and the integer linear programming method. Then, the measurements collected by the MUs placed by both methods were used as inputs to the KF-based DHSE.

Only the theoretical aspects of the problem are reported in this paper, but the corresponding numerical applications are provided in the companion paper [29]. The companion paper compares the two methods for the optimal placement of MUs in terms of: (i) number of required measurements to guarantee the observability of the system; (ii) accuracy of the corresponding KF-based DHSE; and (iii) computational burden.

## ACKNOWLEDGMENTS

This work was supported by Ministero dell'Istruzione dell'Università e della Ricerca (MIUR) in the frame of PON03PE\_00178\_1: Microgrid Ibride in Corrente Continua e

Corrente Alternata (MICCA). The authors also thank Prof. Guido Carpinelli for his constructive support in the realization of this work.

## REFERENCES

- [1] E. Santacana, G. Rackliffe, and Xiaoming Feng. "Getting Smart," *IEEE Power and Energy Magazine*, **8**, pp. 41-48, 2010
- [2] H. Farhangi. "The Path of the Smart Grid," *IEEE Power and Energy Magazine*, **8**, pp. 18-28, 2010
- [3] N. Hatziaargyriou, H. Asano, R. Iravani, and C. Marnay, "Microgrids," *IEEE Power and Energy Magazine*, **5**, pp. 78-94, 2007
- [4] K. Kurohane, T. Senjyu, A. Yona, N. Urasaki, T. Goya, and T. Funabashi. "A Hybrid Smart AC/DC Power System," *IEEE Transactions on Smart Grid*, **1**, pp.199-204, 2010
- [5] L. Alfieri, G. Carpinelli, D. Proto, and G. Russo. "Day-ahead Optimal Scheduling of Loads and Dispatchable Resources in a Hybrid AC/DC Microgrid of an Industrial System," *ICREPO' 15*, La Coruña, Spain, March 25--27, 2015
- [6] A. Griffio, G. Carpinelli, D. Lauria, and A. Russo. "An optimal control strategy for power quality enhancement in a competitive environment," *International Journal of Electrical Power & Energy Systems*, **29**, pp. 514-525, 2007
- [7] P.T. Baboli, M. Shahparasti, M.P. Moghaddam, M.R. Haghifam, and M. Mohamadian. "Energy management and operation modeling of hybrid AC-DC microgrid," *IET Generation, Transmission & Distribution*, **8**, pp. 1700-1711, 2014
- [8] U. Arumugam, N. M. Nor, and M. F. Abdullah. "A Brief Review on Advances of Harmonic State Estimation Techniques in Power Systems," *International Journal of Information and Electronics Engineering*, **1**, pp. 217-222, 2011
- [9] M. Najjar and G. T. Heydt. "A hybrid nonlinear-least squares estimation of harmonic signal levels in power systems," *IEEE Transactions on Power Delivery*, **6**, pp. 282–288, 1991.
- [10] M. Hurtgen and J. C. Maun. "Advantages of power system state estimation using Phasor Measurement Units," in *Proceedings of the 16th Power Systems Computation Conference (PSCC '08)*, Glasgow, Scotland, July, 2008
- [11] H. M. Beides and G. T. Heydt. "Dynamic state estimation of power system harmonics using Kalman filtering methodology," *IEEE Transaction on Power Delivery*, **6**, pp. 1663– 1669, 1991
- [12] H. Ma, and A.A. Girgis. "Identification and tracking of harmonic sources in a power system using a Kalman filter," *IEEE Trans Power Delivery*, **11**, pp. 1659–65, 1996
- [13] A.P. Sakis Meliopoulos, F. Zhang, and S. Zelingher. "Power system harmonic state estimation," *Proceedings of IEEE/PES winter meeting*, New York, USA, 1994.
- [14] V.L. Pham, K.P. Wong, N. Watson, and J. Arrillaga. "Sub-harmonic state estimation in power systems," *IEEE Power Eng Soc Winter Meet*, **2**, pp. 1168–1173, 2000
- [15] J. Sexauer, P. Javanbakht, and S. Mohagheghi. "Phasor measurement units for the distribution grid: Necessity and benefits," *Innovative Smart Grid Technologies (ISGT), 2013 IEEE PES*, Feb. 24–27, 2013
- [16] G. Sanchez-Ayala, J.R. Aguerc, D. Elizondo, and M. Lelic. "Current trends on applications of PMUs in distribution systems," *Innovative Smart Grid Technologies (ISGT), 2013 IEEE PES*, Feb. 24–27, 2013
- [17] W. Yuill, A. Edwards, S. Chowdhury, and S.P. Chowdhury. "Optimal PMU placement: A comprehensive literature review," *Power and Energy Society General Meeting, 2011 IEEE*, July 24--29, 2011
- [18] K.K. More, and H.T. Jadhav. "A literature review on optimal placement of phasor measurement units," *Power, Energy and Control (ICPEC), 2013 International Conference on*, Feb. 6–8, 2013
- [19] H.G. Abood, and V. Sreeram. "A review on phasor measurement units placement for state estimation studies," *Power Engineering Conference (AUPEC), 2014 Australasian Universities*, Sept. 28 -- Oct. 1, 2014
- [20] R. Lukomski and K. Wilkosz. "Methods of measurement placement design for power system state estimation," *AT&P JPLUS 2, POWER Syst. Model. Control*, 2008
- [21] F. J. Marin, F. Garcia-Lagos, G. Joya, and F. Sandoval, "Genetic algorithms for optimal placement of phasor measurement units in electric networks," *Electron. Lett.*, **39**, pp. 1403-1405, 2003
- [22] F. Aminifar, C. Lucas, A. Khodaei, and M. Fotuhi-Firuzabad. "Optimal placement of phasor measurement units using immunity genetic algorithm," *IEEE Trans. Power Syst.*, **24**, pp.1014-1020, 2009
- [23] M. Hajain, A. M. Ranjbar, T. Amraee, and A. R. Shirani. "Optimal placement of phasor measurement units: Particle swarm optimization approach," in *Proc. Int. Conf. Intelligent Systems and Applications in Power Systems*, pp. 1-6, 2007
- [24] S. Chakrabarti, and E. Kyriakides. "Optimal placement of phasor measurement units for power system observability," *IEEE Trans. Power Syst.*, **23**, pp. 1433-1440, 2008
- [25] C. Madtharad, S. Premrudeepreechacharn, N.R. Watson, and Ratchai Saeng-Udom. "An optimal measurement placement method for power system harmonic state estimation," *IEEE Transactions on Power Delivery*, **20**, pp. 1514-1521, 2005
- [26] B. Xu and A. Abur. "Observability analysis and measurement placement for system with PMUs," in *Proc. IEEE Power System Conf. Expo.*, **2**, pp. 943-946, 2004
- [27] F. Aminifar, M. Shahidehpour, M. Fotuhi-Firuzabad, and S. Kamalnia. "Power system dynamic state estimation with synchronized phasor measurements," *IEEE Trans. Power Syst.*, **63**, pp. 352–363, 2014
- [28] K.K.C. Yu, N.R. Watson, and J. Arrillaga. "An adaptive Kalman filter for dynamic harmonic state estimation and

harmonic injection tracking," *IEEE Transactions on Power Delivery*, **20**, pp. 1577-1584, 2005

- [29] L. Alfieri, A. Bracale, P. De Falco, and M. Aprea. "On the comparison among optimal measurement placement methods for a hybrid micro grid harmonic state estimation. Part II: Numerical Applications," in *Proceedings of 3rd International Symposium on Energy Challenges and Mechanics*, Aberdeen, Scotland, UK, July 7-9, 2015



# On the comparison among optimal measurement placement methods for a hybrid microgrid harmonic state estimation. Part II: numerical applications

## 关于混合微电网谐波状态估计的最佳测量选择方法之比较。第二部分：数值应用

L. Alfieri<sup>1\*</sup>, A. Bracale<sup>2</sup>, P. De Falco<sup>1</sup>, M. Aprea<sup>1</sup>

<sup>1</sup>*Department of Electrical Engineering and of Information Technology, University of Naples Federico II, Naples - 80125, Italy*

<sup>2</sup>*Department of Engineering, University of Naples Parthenope, Naples - 80143, Italy*

*luisa.alfieri@unina.it*

Accepted for publication on 12<sup>th</sup> October 2015

**Abstract** – This is a companion paper to the Part I paper, in which the theoretical aspects of the optimal measurement units (MUs) placement for the dynamic harmonic state estimation (DHSE) on a hybrid AC/DC micro grid ( $\mu$ G) are analyzed. In particular, Part I dealt with two techniques, available in the relevant literature, for the optimal MUs placement; these techniques, based on the minimum condition number of the measurement matrix and on the integer linear programming, were properly used to obtain the measurements needed as inputs for the DHSE with a Kalman filter (KF). In this paper, numerical applications are presented, in order to compare the two methods in terms of: (i) number of required measurements to guarantee the observability of the system; (ii) the accuracy of the corresponding KF-based DHSE; (iii) computational burden. The numerical experiments were performed on a hybrid AC/DC  $\mu$ G proposed for an actual industrial facility in southern Italy.

**Keywords** - Optimal measurement placement, dynamic harmonic state estimation, Kalman filter, micro grid, power quality.

### I. INTRODUCTION

In the context of modern smart grids (SGs) and micro grids ( $\mu$ Gs), the dynamic state estimation (DSE) is a concerning issue, since it was proved that it is a fundamental step for the optimal operation of the system [1-3]. The estimates of the state of the system are used as input data for different tasks; for example, to satisfy increasing needs in terms of required Power Quality (PQ) in the considered grid [4-5]. The PQ problem solution is of great interest in SGs and  $\mu$ Gs, since specific PQ requirements must be verified for sensitive loads.

The aim of the companion paper [6] was to propose a method for the dynamic harmonic state estimation (DHSE) on

a hybrid AC/DC  $\mu$ G, using a limited number of measurements as input data, in order to guarantee affordable installation and maintenance costs. The DHSE was performed through one of the most common methods proposed in the relevant literature [7]. In particular, the method proposed in [4], based on the Kalman filter (KF), was used.

In the companion paper [6] the measurements were properly selected using two techniques for the optimal measurement units (MUs) placement, available in literature [8-11]. Both techniques guarantee the observability of the system, and select the minimum number of MUs on the basis of the minimum condition number of the measurement matrix and on the basis of the integer linear programming approach, respectively. In this paper, numerical applications of the aforesaid placement methods were performed on an hybrid AC/DC  $\mu$ G proposed for an actual industrial facility in southern Italy. First, a comparison between the two optimal MUs placement methods was performed on the basis of the number of required measurements and of the computational burden. Then, the selected measurements were used as input data for the KF-based DHSE, and a further comparison was performed in terms of estimates accuracy. The DHSE results were compared also with the results of a limit case in which all of the measurements were assumed to be available.

The remainder of this paper is organized as follows. In Section II a brief description of the hybrid AC/DC  $\mu$ G is provided. In Section III the results of the optimal MUs placement methods are presented, while in Section IV the results of the KF-based DHSE are shown and discussed. Our conclusions are reported in Section V. In the Appendix, additional data about the analysed hybrid  $\mu$ G are provided.

## II. THE HYBRID AC/DC $\mu$ G

The optimal MUs placement procedures, shown in Section III of the companion paper [6], and the DHSE illustrated in

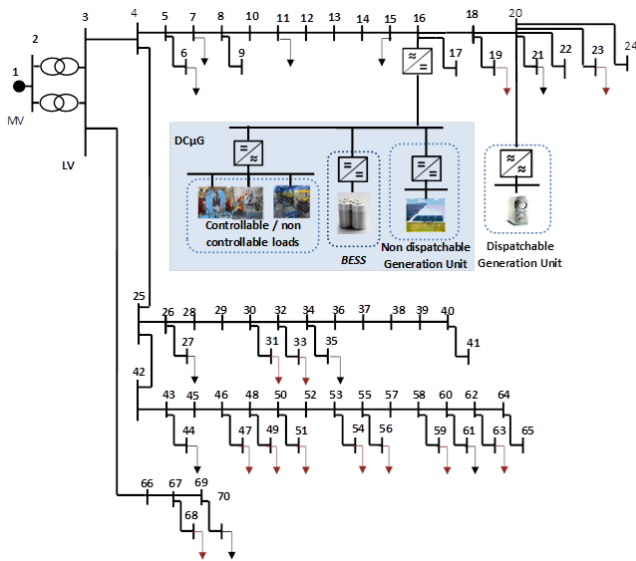


Fig. 1, Hybrid AC/DC  $\mu$ G.

The  $\mu$ G in Fig. 1 was proposed for an actual electrical distribution system of an industrial facility located in southern Italy. The original network is connected to the national MV distribution grid through two 630 kVA MV/LV transformers (20/0.4 kV), and includes four LV feeders, one for each different manufacturing process line. The total number  $N$  of buses is 70. The proposed AC/DC  $\mu$ G includes three controllable loads, a PV generation plant, a gas micro turbine generator and a battery energy storage system (BESS). As shown in Fig. 1, an AC/DC static converter, placed in bus #16, connects the DC side to the AC side of the  $\mu$ G; the micro turbine is located at bus #20. The red (black) arrows in Fig. 1 correspond to non-linear loads (linear loads). Tab.1 provides for non-linear loads (Tab. 1a) and linear loads (Tab. 1b): the bus allocation, the description of the industrial machine type, the rated power and the power factor.

Line parameters are reported in the Appendix. The hybrid  $\mu$ G was simulated in MATLAB-Simulink environment, and the programs were developed and tested on a Windows PC with an Intel i7-3770 3.4 GHz and 16 GB of RAM. In the following, the results obtained by applying the proposed approaches are shown.

## III. OPTIMAL MUS PLACEMENT METHODS

The optimal MUs placements obtained by using the minimum condition number method (MCNM) and the integer linear programming method (ILPM) are reported and compared with a limit case, in which all of the state variables are measured (AM).

Section IV of [6], were applied to the AC/DC hybrid  $\mu$ G shown in Fig. 1.

With reference to the MCNM (Section 3.1 of the companion paper [6]), the measurement matrix for the fundamental component  $\hat{H}(1)$  was determined from the admittance matrix  $\hat{Y}_{NN}(1)$  and from the line-bus admittance matrix  $\hat{Y}_{LN}(1)$ , that can be both obtained from the knowledge of the equivalent circuit of the system.

TABLE 1, (A) NON-LINEAR LOADS; (B) LINEAR LOADS.

Bus	Type	Rated Power [kVA]	Power Factor
16	Sandblaster	55	0.75
16	Folding walls island robot	24	0.99
16	PLC + computer	3	0.62
19	Wave welding machine	30	0.65
23	Plasma cutting machine	15	0.8
31, 33	Core cutting machine n.1	60	0.8
47, 49, 51	MT winder machine	37	0.99
54, 56	Tuboly winder machine	37	0.99
59, 63	BT winder machine	37	0.99
68	Bender machine + robot	20	0.9

(A)

Bus	Type	Rated Power [kVA]	Power Factor
6	Painting machine	75	0.8
7	Box overturning machine	4	0.99
11	Welder aspirators	11	0.99
15	Manual bender	8	0.99
21	Corrugated walls machine	122	0.65
27	Crane	5.5	0.8
35	Autoclaves	86	0.8
44	Furnace	5	0.99
61	Offices	36	0.99
70	Testing bench room	50	0.7

(B)

With reference to the ILPM (Section 3.2 of the companion paper [6]), the binary transformation of the bus-bus admittance matrix into the connectivity matrix  $\mathbf{S}$  was performed, in order to define the constraints of the optimization problem. The weight factors  $w_i$  in the objective function were all assumed to be unitary. In fact, since there were no preferential buses for the MUs placement, the weight factors could be considered all equal.

The results of both methods, in terms of the minimum number of MUs to be installed and the number of state variables to be measured, are reported in Tab. 2, together with the data of the AM case.

Tab. 2 shows that both the MCNM and the ILPM require the same number of MUs to be installed, that is less than half of the maximum MUs number (AM case). Moreover, the ILPM requires the acquisition of a greater number of measurements than the MCNM, thus the MUs required in each case should be different in term of input channels. Note that the number of required line currents is the same for the MCNM and the ILPM, while the numbers of measured bus voltages and load currents are different.

Note that, as stated in Section 3.1 of the companion paper [6], the results of the MCNM in Tab. 2 were obtained considering only the measurement matrix for the fundamental component ( $h = 1$ ). This choice was due to a preliminary sensitivity analysis, performed by considering each harmonic (including the fundamental component) separately and all harmonics together, as in [10]. Some results of the sensitivity analysis are reported in Tab. 3, on the basis of the number and the type of state variables to be measured.

From the analysis of Tab. 3 it is possible to note that, as the harmonic order  $h$  increases, the number of measured line currents and load currents decrease, while the number of measured bus voltages increases.

The MCNM, applied for all of the combined harmonic orders, requires the highest number of measurements, and therefore appears to be redundant to achieve the observability of the system. As shown in Section IV, the solution based on the fundamental component led to the best results in terms of estimates accuracy in our application.

Eventually, Tab. 4 shows the average computational time required by both the selected placement methods. It is clear that the ILPM requires the smallest amount of time to solve the optimization problem; the MCNM applied to fundamental component performs an iterative procedure for the reduction of the measurement matrix, and therefore is slower. In particular, the ILPM time is about 1/35 of the MCNM time.

TABLE 2, COMPARISON BETWEEN THE RESULTS OF THE OPTIMAL MUS PLACEMENT METHODS.

	Method		
	MCNM	ILPM	AM
Number of MUs	31	31	68
Number of measured line currents	60	60	68
Number of measured bus voltages	0	26	68
Number of measured load currents	8	0	68
Total number of measurements	68	86	204

TABLE 3, COMPARISON BETWEEN THE RESULTS OF THE MCNM FOR DIFFERENT HARMONIC ORDERS.

Selected harmonic order
-------------------------

	1-st	5-th	7-th	11-th	13-th	All
Number of measured line currents	60	13	11	1	1	60
Number of measured bus voltages	0	55	57	67	67	67
Number of measured load currents	8	0	0	0	0	8

TABLE 4, AVERAGE COMPUTATIONAL TIME OF THE SELECTED PLACEMENT METHODS.

	Method	
	MCNM	ILPM
Average computational time [s]	19.47	0.56

#### IV. DYNAMIC HARMONIC STATE ESTIMATION WITH KALMAN FILTER

The measurements taken through the MCNM, the ILPM and AM were separately considered as inputs for the KF-based DHSE. The DHSE, according to the model (17) of the companion paper [6], was performed to estimate the harmonic disturbances of order  $h = 5, 7, 11, 13$ , which usually are among the most significant disturbances in a distribution system. Measured and estimated disturbances in all of the buses where a non-linear load is placed were compared; however, for sake of conciseness, in this paper only the comparison of the disturbances in buses #23 and #54 are reported. Note that the harmonic disturbances, introduced in the  $\mu\text{G}$  by non-linear loads were directly measured from the original factory distribution system.

Note that buses #23 and #54 were selected since the corresponding load currents present different harmonic contents, so it is possible to evaluate the robustness of the KF-based DHSE on different load conditions. The spectra of the current waveforms at bus #23 and bus #54, are shown in Figs. 2a and 2b, respectively. These spectra were obtained by applying the Discrete Fourier Transform, according to the IEC standard [12-13].

From the analysis of Fig. 2, the differences in terms of harmonic components are evident. In particular, the most significant components of the spectrum in Fig. 2a are the 5-th, 7-th, 11-th and 13-th harmonics; therefore, the adopted model is consistent with the effective spectral content. On the other hand, the higher-order harmonics of the spectrum in Fig. 2b are not negligible, being their amplitudes of the same order of magnitude of the 11-th and 13-th harmonics; therefore, the model used to represent the disturbances appears incomplete.

The estimates of the waveforms at buses #23 and #54, obtained with the KF-based DHSE coupled to the MCNM, the ILPM and AM are shown in Figs. 3a-4a, 3b-4b and 3c-4c,

respectively. The analysis of Figs. 3 and 4 reveals that KF estimates with the MCNM are better than KF estimates with the ILPM. This difference is magnified when an incomplete disturbance model is used (Fig. 4) since the results obtained with the ILPM are significantly poorer than the results obtained with the MCNM. A different behaviour is detected also for AM, which provides the best results when the disturbance model is incomplete (Fig. 4c); this could be due to the corrective effect of all of the measurements taken from the  $\mu$ G. On the other hand, when the model properly fits the measured waveform, the presence of all of the measurements may cause a worsening effect on the aggregate estimates (Fig. 3c).

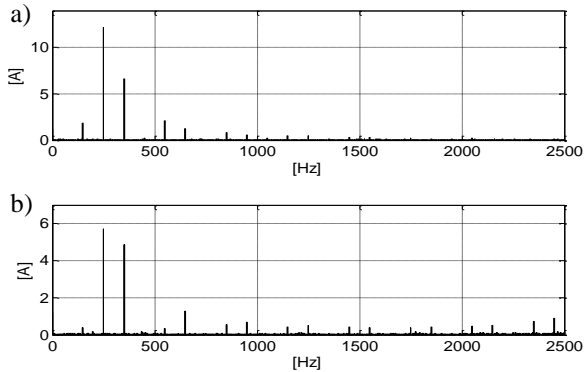


Fig. 2, Spectra of the current waveforms deprived of the fundamental component. Bus #23 (a); Bus #54 (b).

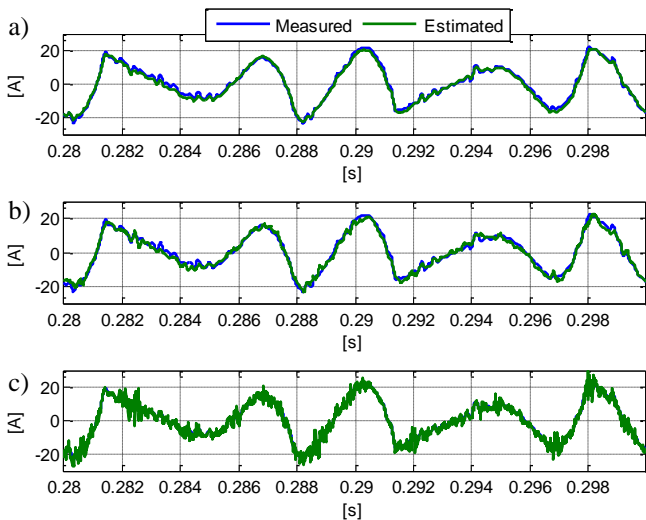


Fig. 3, Bus #23: comparison between actual and estimated current waveforms. KF combined to (a) MCNM, (b) ILPM, (c) AM.

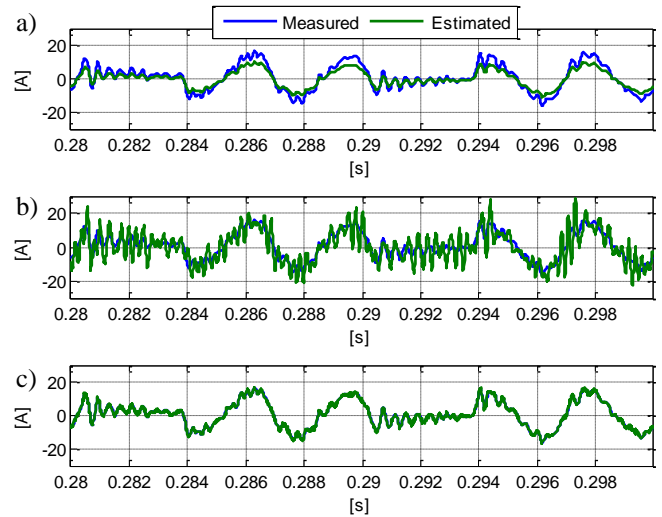


Fig. 4, Bus #54: comparison between actual and estimated current waveforms. KF combined to (a) MCNM, (b) ILPM, (c) AM.

For sake of completeness, Tab. 5 shows the percentage reconstruction errors, related to the waveforms in Figs. 3 and 4, calculated as  $e_{\%} = \frac{1}{N} \sum_i \left| \frac{x_i - \hat{x}_i}{x_{max}} \right| \cdot 100$ , where  $x$  is the measured disturbance vector,  $\hat{x}$  is the estimated disturbance vector and  $x_{max}$  is the maximum value of  $x$ . From the analysis of Tab. 5, it clearly appears that the errors on the aggregate estimates at bus #23 with the MCNM and the ILPM are comparable; instead, the ILPM error at bus #54 is almost double than the MCNM error. The AM error is greater than both MCNM and ILPM errors at bus #23, while it is significantly lower than them (about 1/6 and 1/11, respectively) at bus #54.

TABLE 5, PERCENTAGE RECONSTRUCTION ERRORS

Method	$e_{\%}$	
	Bus #23	Bus #54
KF with MCNM	4.45	13.86
KF with ILPM	5.99	27.09
KF with AM	7.22	2.45

A further comparison between the results of the KF-based DHSE was effected in terms of reconstruction error for each harmonic order that was considered in the model. For sake of conciseness, in Tab. 6 only the reconstruction errors related to the harmonic components of the disturbance in the bus #23 are reported. From the analysis of these values, it can be noted that for both KF with the ILPM and KF with the MCNM the reconstruction errors increase as the harmonic order increases, since the amplitude of the harmonic component decreases, as shown in Fig. 2a. In particular, KF with the ILPM provides the least accurate estimates of each harmonic component, while KF with the MCNM appears to be the best solution for the DHSE. KF with AM supplies accurate estimates at each harmonic, although it provided the worst aggregate waveform estimate, as reported in Tab. 5. This was due to the introduction of high-frequency components during the

dynamic estimation, as shown in Fig. 3c; these high-frequency components obviously affect the aggregate reconstruction error, but do not invalidate the single harmonic estimates.

TABLE 6, COMPARISON BETWEEN THE ERROR

	$e_{\%}$			
	5-th	7-th	11-th	13-th
KF with MCNM	0.11	0.30	0.35	0.81
KF with ILPM	1.72	5.97	8.79	14.73
KF with AM	0.74	0.99	0.31	1.49

Finally, the sensitivity analysis on the performances of the MCNM for different harmonic orders (including the fundamental component), and for all of the combined harmonic orders, was performed on the basis of the corresponding DHSE accuracy, as previously evidenced. For sake of conciseness, only the comparison between the results obtained applying MCNM at the 1-st and 7-th harmonic orders, and for all of the combined harmonic orders are shown in Tab. 7, for both the previously considered buses.

From the analysis of the reconstruction errors in Tab. 7, the DHSE with the measurements provided by the MCNM at the fundamental component seems to be the most reliable, since it shows the best performances when the disturbance is well-modelled (bus #23), and it still shows a satisfying accuracy when the disturbance is not well-modelled (bus #54). Moreover, for the disturbance at bus #54, we note that the error of the DHSE with the MCNM at all of the combined harmonic orders is similar to the error of the DHSE with the MCNM at the fundamental component. For the disturbance at bus #23, the error of the DHSE with the MCNM at all of the combined harmonic orders increases significantly, although the global number of measurements increases. This is coherent with the results obtained in Tab.5 for the AM case. On the other hand, the results obtained by MCNM at the 7-th harmonic seem to be globally inaccurate.

TABLE 7, COMPARISON OF THE RESULTS OF THE MCNM, FOR DIFFERENT HARMONIC ORDERS, IN TERMS OF DHSE ACCURACY

Selected harmonic order	$e_{\%}$	
	Bus #23	Bus #54
1-st	4.45	13.86
7-th	7.99	42.20
All	20.96	13.47

### V. CONCLUSIONS

This paper provides an application of the DHSE on a hybrid AC/DC  $\mu$ Gs. The DHSE is performed through a KF-based approach. The necessary measurements required in the KF are obtained from MUs, which have been placed on the basis of the results of two optimal placement methods, commonly used for AC networks: the minimum condition number method and the integer linear programming method.

The performances of each placement method and of the correspondent DHSE were compared in terms of: (i) number of required measurements to guarantee the observability of the system; (ii) accuracy of the corresponding KF-based DHSE; (iii) computational burden. Moreover, a limit case, in which the measurements of all of the state variables were available, was also considered.

The methods were tested on a hybrid AC/DC  $\mu$ G proposed for an actual industrial facility located in southern Italy. The numerical applications showed that the results obtained by using the measurements provided by the MCNM as input data for the DHSE were generally better than the results obtained with the measurement provided by ILPM. Moreover, both methods allowed a reliable DHSE in presence of a reduced number of measurements, thus reducing the total costs for the installation of MUs. In terms of computational burden, MNCM appeared more onerous than ILPM.

### APPENDIX

In the following, the data of the lines of the hybrid AC/DC  $\mu$ G are provided. Specifically, for each line, the starting and ending buses, the length, the resistance and the reactance per unit length are shown in Tabs. 8, 9, 10, 11.

TABLE 8, LINE PARAMETERS FOR THE FIRST FEEDER OF THE PLANT

Buses		$\ell$ [m]	$R$ [m $\Omega$ /m]	$X$ [m $\Omega$ /m]
from	to			
3	4	8	0.041	0.014
4	5	24	0.163	0.130
5	6	4	0.473	0.101
5	7	0.5	0.163	0.130
7	8	6	0.163	0.130
8	9	10	1.410	0.112
8	10	9.3	0.163	0.130
10	11	3	0.163	0.130
11	12	2.8	0.163	0.130
12	13	3.5	0.163	0.130
13	14	3.5	0.163	0.130
14	15	11	0.163	0.130
15	16	19.1	0.163	0.130
16	17	4	1.410	0.112
16	18	1.9	0.163	0.130
18	19	4	1.410	0.112
18	20	3	0.163	0.130
20	21	10	0.236	0.097
20	22	42	1.410	0.112
20	23	61	2.240	0.119
20	24	61	1.410	0.112

TABLE 11, LINE PARAMETERS FOR THE FOURTH FEEDER OF THE PLANT

Buses		$\ell$ [m]	R [mΩ/m]	X [mΩ/m]
From	to			
2	66	30	0.094	0.090
66	67	87	0.163	0.130
67	68	7	1.410	0.112
67	69	0.5	0.163	0.130
69	70	7	0.473	0.101

TABLE 9, LINE PARAMETERS FOR THE SECOND FEEDER OF THE PLANT

Buses		$\ell$ [m]	R [mΩ/m]	X [mΩ/m]
from	to			
4	25	31	0.041	0.014
25	26	3.5	0.163	0.130
26	27	16	2.240	0.119
26	28	9	0.163	0.130
28	29	12.5	0.163	0.130
29	30	10.5	0.163	0.130
30	31	8	0.641	0.101
30	32	1.5	0.163	0.130
32	33	10	0.641	0.101
32	34	12.5	0.163	0.130
34	35	8	0.328	0.096
34	36	13	0.163	0.130
36	37	1	0.163	0.130
37	38	35	0.665	0.260
38	39	0.5	0.665	0.260
39	40	0.5	0.665	0.260
40	41	20	1.410	0.112

TABLE 10, LINE PARAMETERS FOR THE THIRD FEEDER OF THE PLANT

Buses		$\ell$ [m]	R [mΩ/m]	X [mΩ/m]
From	to			
25	42	34	0.041	0.014
42	43	3.3	0.070	0.096
43	44	12	2.240	0.119
43	45	9.2	0.070	0.096
45	46	5.5	0.070	0.096
46	47	5.5	1.410	0.112
46	48	6.5	0.070	0.096
48	49	5.5	1.410	0.112
48	50	7.8	0.070	0.096
50	51	5.5	1.410	0.112
50	52	5.2	0.070	0.096
52	53	1.8	0.070	0.096
53	54	5.5	1.410	0.112
53	55	8.1	0.070	0.096
55	56	5.5	1.410	0.112
55	57	5.6	0.070	0.096
57	58	4.5	0.070	0.096
58	59	5.5	1.410	0.112
58	60	3	0.070	0.096
60	61	8	0.473	0.101
60	62	2.5	0.070	0.096
62	63	5.5	1.410	0.112
62	64	3.7	0.070	0.096
64	65	38	1.410	0.112

ACKNOWLEDGMENTS

This work was supported by Ministero dell'Istruzione dell'Università e della Ricerca (MIUR) in the frame of PON03PE\_00178\_1: Microgrid Ibride in Corrente Continua e Corrente Alternata (MICCA). The authors also thank Prof. Guido Carpinelli for his constructive support in the realization of this work.

REFERENCES

- [1] A. Jain, and N.R. Shivakumar. "Impact of PMU in dynamic state estimation of power systems," *Power Symposium, 2008. NAPS '08. 40th North American*, vol., no., pp.1,8, 28-30 Sept. 2008
- [2] N.R. Shivakumar, and A. Jain. "A Review of Power System Dynamic State Estimation Techniques," *Joint International Conference on Power System Technology and IEEE Power India Conference, POWERCON 2008.*, Oct. 12—15, 2008
- [3] E. Ghahremani, and I. Kamwa. "Dynamic State Estimation in Power System by Applying the Extended Kalman Filter With Unknown Inputs to Phasor Measurements," *IEEE Transactions on Power Systems*, **26**, pp. 2556-2566, 2011
- [4] A. Griffio, G. Carpinelli, D. Lauria, and A. Russo. "An optimal control strategy for power quality enhancement in a competitive environment," *International Journal of Electrical Power & Energy Systems*, **29**, pp. 514-525, 2007
- [5] P.T. Baboli, M. Shahparasti, and M.P. Moghaddam, M.R. Haghifam, M. Mohamadian, "Energy management and operation modeling of hybrid AC-DC microgrid," *IET Generation, Transmission & Distribution*, **8**, pp. 1700-1711, 2014
- [6] L. Alfieri, A. Bracale, P. De Falco, and M. Aprea. "On the comparison among optimal measurement placement methods for a hybrid micro grid harmonic state estimation. Part I: Theoretical Aspects," in *Proceedings of 3rd International Symposium on Energy Challenges and Mechanics*, Aberdeen, Scotland, UK, July 7-9, 2015
- [7] U. Arumugam, N. M. Nor, and M. F. Abdullah, "A Brief Review on Advances of Harmonic State Estimation Techniques in Power Systems," *International Journal of Information and Electronics Engineering*, **1**, pp. 217-222, 2011

- [8] W. Yuill, A. Edwards, S. Chowdhury, and S.P. Chowdhury, "Optimal PMU placement: A comprehensive literature review," *Power and Energy Society General Meeting, 2011 IEEE*, July 24–29, 2011
- [9] K.K. More, H.T. Jadhav. "A literature review on optimal placement of phasor measurement units," *International Conference on Power, Energy and Control (ICPEC)*, pp. 220-224, Feb. 6–8, 2013
- [10] C. Madtharad, S. Premrudeepreechacharn, N.R. Watson, and Ratchai Saeng-Udom. "An optimal measurement placement method for power system harmonic state estimation," *IEEE Transactions on Power Delivery*, **20**, pp. 1514-1521, 2005
- [11] B. Xu, and A. Abur. "Observability analysis and measurement placement for system with PMUs," in *Proc. IEEE Power System Conf. Expo.*, **2**, pp. 943-946, 2004
- [12] *Testing and measurement techniques – Power quality measurement methods*. IEC standard 61000-4-30, 2008
- [13] *General guide on harmonics and interharmonics measurements, for power supply systems and equipment connected thereto*. IEC standard 61000-4-7, 2009



# Time varying waveform distortions caused by dispersed generators in Smart Grids

## 由智能电网中分散发电机所导致的随时间变化之波形失真

L. Alfieri<sup>1\*</sup>, A. Bracale<sup>2</sup>

<sup>1</sup>*Department of Electrical Engineering and of Information Technology, University of Naples Federico II, Naples - 80125, Italy*

<sup>2</sup>*Department of Engineering, University of Naples Parthenope, Naples - 80143, Italy*

*[luisa.alfieri@unina.it](mailto:luisa.alfieri@unina.it)*

Accepted for publication on 12<sup>th</sup> October 2015

**Abstract** - Among power quality disturbances, the distortions of voltage and current waveforms are turning into one of the most important issues, due to the great diffusion of electronic power converters used to supply loads or interconnect the distributed energy resources (DER) to the grid. In particular, wind turbines systems (WTS) and photovoltaic systems (PVS) are the most extensively used DER in the actual active distribution networks, and these systems are expected to rise fast in the future smart grids (SGs) as a result from the forecasted economic advantages. This paper provides a review of the theoretical aspects about the most common PVS and WTS configurations and about the waveform distortions introduced by both these systems at the point of common coupling in several operating conditions. Numerical applications are also performed by applying an advanced spectral analysis method which seems particularly suitable to capture the time-varying nature of the current and voltage waveforms of the systems under study.

**Keywords** - Smart grid, power quality, waveform distortions, wind turbine systems, photovoltaic systems.

### I. INTRODUCTION

Currently, the interest towards the Power Quality (PQ) disturbances is growing since adequate PQ levels guarantee the necessary compatibility between all of the equipment connected to the grid. In particular, in the smart grids (SGs) context, the distortions of voltage and current waveforms are turning into one of the most important issue, due to the great diffusion of the electronic power converters to supply loads or to interconnect the distributed energy resources (DER) to the grid [1-4].

Indeed, the widespread use of DER in SGs contributes significantly to the waveform distortions which can be not acceptable for sensitive loads. In particular, wind turbines systems (WTS) and photovoltaic systems (PVS) are the most extensively used DERs in the actual distribution networks, and these systems are expected to rise fast in the future SGs, as a result from the forecasted reduction in investment costs and to other economic incentives.

Different configurations are available to connect WTSs and PVSs to the grid; each of them can generate time-varying voltage and current waveform distortions characterized by spectral components at low and high frequencies, which can reach significant magnitudes in specific operating conditions [3-4]. Therefore, the study of their impact on the distribution networks is a topic of great interest and widely discussed in the relevant literature [5].

Motivated by the aforesaid considerations, the main objective of this paper is to provide an overview of the most common PVS and WTS configurations and of the waveform distortions introduced by these systems at the point of common coupling (PCC) in several operating conditions [6-16].

The theoretical aspects of the problems are enriched by numerical applications on actual current waveforms. The numerical experiments are performed by applying the advanced spectral analysis method proposed in [17], based on modifications of the ESPRIT signal models; this method was proved to be particularly suitable to capture the time-varying nature of the current and voltage waveforms introduced by the

systems which are aim of our study, also requiring a reduced computational effort.

This paper is organized as follows. Section II briefly describes the different PVS and WTS schemes, discussing the typical waveform distortions caused by each of these systems. In Section III the advanced method proposed in [17] is briefly recalled and in Section IV numerical experiments are shown, comparing the spectra obtained by using the proposed method with the spectra that are theoretically expected. Conclusions are presented in Section V.

## II. WAVEFORM DISTORTION IN THE MOST COMMON SCHEME OF PV AND WT SYSTEMS

It is well known that active distribution networks are experiencing the widespread use of DERs and that the most diffuse sources of renewable energy are solar and wind plants. In this section, an overview of the most common PVS and WTS schemes is provided, paying particularly attention to the waveform distortions caused by each of them.

In particular, primary and secondary spectral emissions are considered: the first typology refers only to the distinctive disturbances of the considered system; the second typology of emissions refers to the disturbances caused by other sources near the system (i.e., non-linear loads and power communication signals) [14].

Moreover, the spectra of voltage and current waveforms at the PCC of both PVSs and WTSs include a wide range of frequencies. For the sake of clarity, in the following, the spectral components are classified as “low-frequency components” (up to 2 kHz) and “high-frequency components” (over 2 kHz).

### 2.1. PHOTOVOLTAIC SYSTEM

A PVS is connected to the grid through inverters, that, basically, realize the DC/AC conversion of the electric energy, fulfilling particular specifications in terms voltage and frequency. The photovoltaic inverters are among the most advanced electronic power converters, since they are controlled in order to perform important tasks, such as the maximum power point tracking, the anti-islanding and the grid synchronization; therefore their functionalities must be improved with respect, for instance, to motor drive inverters, and this fact influences their hardware complexity [6,13, 18].

Based on the typologies of the inverters used, the PVSs assume different characteristics and benefits, i.e., the large-scale PVSs can be connected to the grid through a three-phase inverter or through three single-phase inverters combined as a “quasi three-phase” inverter. In the first case, no zero-sequence emissions are found in the waveform spectra and the load balancing among the phases is guaranteed, but its efficiency and reliability are poorer than those of the latter solution. In addition, since the large-scale photovoltaic plants could be expanded over time, single-phase inverters prove to be more versatile than three-phase inverters, in order to guarantee an easier spread of the system. In this context, hybrid configurations, such as the multi-string inverters, can

be useful to obtain the combined benefits of the previous configurations [15].

The inverter is the core element of the whole PVS, highly influencing the system efficiency, lifetime and size; many research activities focused on its improvement and development, making available a large variety of photovoltaic inverters. Fig. 1 shows the schemes of PVSs connected through (i) inverters with line frequency isolation transformers (Fig. 1a), (ii) inverters with high frequency isolation transformers (Fig. 1b), and (iii) inverters without isolation transformers (Fig. 1c). These are among the most common solutions for the PVSs, and each of them is able to satisfy particular requirements [6, 15].

The first two solutions are suitable when galvanic isolation and voltage step-up are required for the system. The solutions with line frequency transformers provide higher efficiency than those with high frequency transformers, since they need less power stages than the latter, but they are also the most expensive configurations. Single-phase PVS connected through both line-frequency and high-frequency transformers are characterized by primary emissions with relevant third harmonic components, introduced by the magnetizing currents of the transformers. The magnitude of these components significantly increase when the transformer operates over the rated voltage, since, in these operating conditions, the magnetizing currents increase [18, 19].

When the galvanic isolation is not required, an inverter without isolation transformer can be used; it guarantees both economic efficiency and high performances, with primary emissions introduced only by the particular PWM technique used for the inverter control [18, 20].

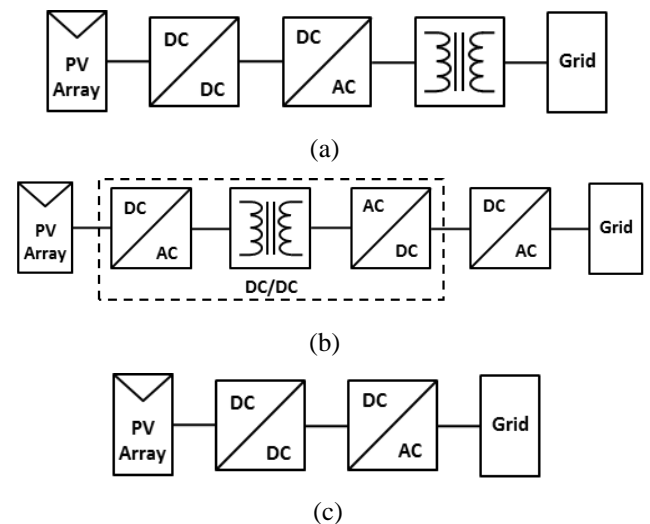


Fig. 1, Schemes of single-phase PVSs: (a) inverter with line-frequency isolation transformer; (b) inverter with high-frequency isolation transformer; (c) inverter without an isolation transformer.

However, different operating conditions of the PVS cause different waveform distortions, which are generally reduced by the presence of the LC filters. Note that the harmonics and interharmonics usually do not change significantly as the PV power changes; however, some harmonics could slightly

increase as the power increases, and the use of multiple inverters in a PVS produces usually lower levels of emissions than the use of an unique, large-size inverter [21].

In particular, in [22] the behavior of the distorting spectral components at the PCC in a 800 kWp-PV plant was analyzed; the PV system is constituted by 16 three-phase inverters and the analysis was performed for two intervals of active power equal to 0÷10% and 90÷100% of rated power respectively. The results showed that for the low-power interval the distortion level was significantly more relevant than for the high-power interval, and the maximum harmonic current levels established according to the IEC standards were overcome in the first scenario [23-24]. However, in both cases only the spectrum up to 50th harmonic was examined, and significant spectral components were detected in correspondence of the 3rd, 5th, 7th and 11th harmonics, and the effects of a parallel resonance were observed over the 20th harmonic, since high values of amplitude were identified. The authors did not provide any information about which specific low-frequency component was due to PWM over-modulation or to background voltages; they only provided the global incidence of the single PVS on the background harmonics at the PCC through the site total harmonic distortion 95% percentile variation ( $STHD_{Uj,95}$ ). Specifically, this index has been estimated equal to 40.12% in the low-power range and equal to 5.18% in the high-power range, suggesting that the background voltages are the main cause of the low-frequency components.

In general, the PVSs spectral emissions at the PCC can include both low- and high-frequency spectral components. The first typology is due to background distortions (secondary emission) or PWM over-modulation of the inverter (primary emission); the amplitudes of low-frequency components in a single photovoltaic plant in rated conditions generally determine a current total harmonic distortion (THDi) lower than 10%; in resonance conditions, significant voltage distortions can be produced, causing heavy problems for the electric network [15].

High-frequency components are mainly due to the PVS inverter and to its particular PWM technique (primary emission). As shown in [25], these high-frequency components are always detected during the hours of power production of the system while, during the night, the inverter is practically turned off and these components disappear. Basically, these components are mostly harmonics and they appear in correspondence of sideband, centered around integer multiples of the inverter switching frequency. Since for commercially-available inverters the switching frequency usually falls in the range [10÷20] kHz, the spectral components introduced by the inverter belong to the supraharmonics category, for which adequate standards are still aims of study of recent research activities [14, 15, 26].

Also high-frequency secondary emissions can be expected: these are due to background voltage and could increase significantly in presence of series resonance effects.

## 2.2. WIND TURBINE SYSTEM

A WTS is basically constituted by a mechanical part and by an electrical part: the first converts the kinetic energy of the wind into mechanical energy, yielding the rotation of a motor shaft; the second part produces electrical energy with characteristics proper to feed the grid [18].

Consistent with the great gamma of WTSs available in commerce, different classifications, based upon both the mechanical and electrical part, can be made: i.e., it is possible to find WTSs with different numbers of blades, with different directions of the rotor axis, or with different speed characteristics. This last classification is the most interesting and includes (Fig. 2): (i) fixed-speed wind turbine systems (Fig. 2a), (ii) semi-variable-speed wind turbine systems with a rotor resistance converter (Fig. 2b), (iii) variable-speed wind turbine systems with the doubly fed induction generators (Fig. 2c) and (iv) variable-speed wind turbine systems with full-scale power converters (Fig. 2d) [13, 27, 28]. Each configuration has specific pros and cons and introduces different harmonic and interharmonic waveform distortions.

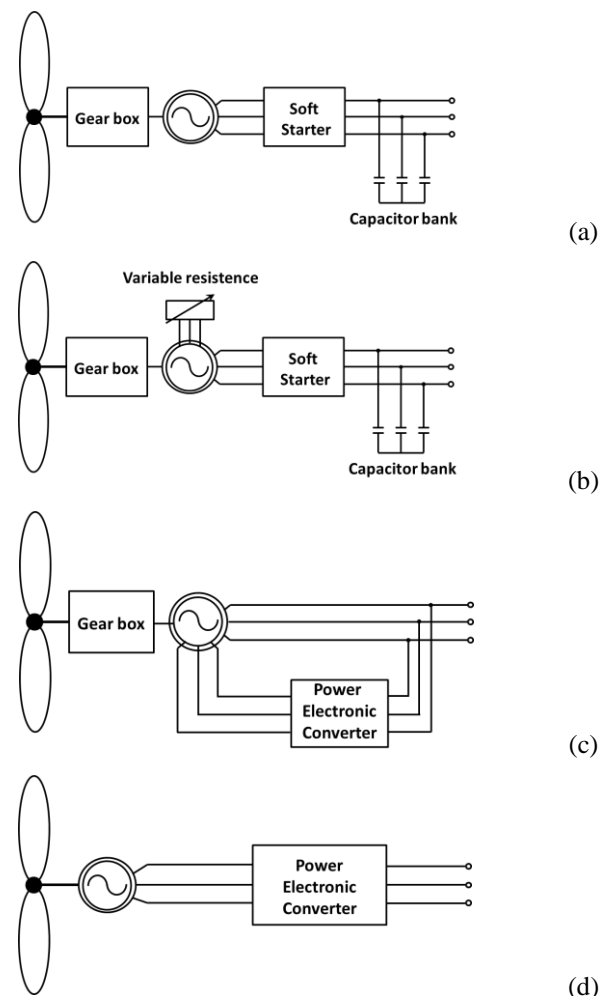


Fig. 2. Schemes of the different Type of WTSs: (a) fixed speed WT; (b) semi variable-speed WT; (c) DFIG WT; (d) full-scale power converter WT.

The first solution (Fig. 2a) is commonly identified as Type-I wind turbine system and it is characterized by the presence of

a gearbox and a squirrel-cage induction generator (SCIG), and by the absence of any power electronic converter. It is linked to the grid by means of a transformer. Generally, this configuration is equipped with an electronic soft-starter, in order to reduce, during the start-up phase, the effect of the in-rush current. Since the SCIG has not an excitation winding, it absorbs reactive power from the network, so a capacitor bank is generally utilized in order to compensate the reactive power [13, 29]. These SCIGs usually work at a nearly-fixed speed, determined mainly by the frequency of the supply grid and by the gear ratio, and it is set above the synchronous speed, according to the SCIG nature. Specifically, since the frequency of the grid is fixed, the only degrees of freedom for the definition of the rotor speed are the gear ratio and the number of poles in the generator. The Type-I wind turbines are cheap and sturdy and they are suitable for a robust frequency control, but they do not guarantee the grid voltage control when an islanding condition occurs; moreover, the wind speed variations are directly turned into electromechanic torque variations, causing mechanical stress [13, 29].

The second configuration (Fig. 2b) is commonly indicated as Type-II wind turbine system and has a structure very similar to the Type-I wind turbines, but it differs for the presence of a wound rotor induction generator (WRIG) with a variable additional rotor resistance, spliced on the rotor shaft and controlled through a converter. Varying this additional resistance, it is possible to control both the power output and the slip of the induction generator, in order to change the rotor speed in a limited range, that is 0÷10% above the synchronous speed [29].

The Type-I and Type-II WTSs are not expected to produce high levels of spectral emissions; therefore, the IEC standards [30] do not specify any particular requirement. However, the action of the soft-starter can produce odd harmonic components at low-frequency, which have low amplitudes and short duration, and triple harmonics can occur in voltage unbalances conditions [31].

The third configuration (Fig. 2c) is commonly identified as Type-III wind turbine system and is characterized by a gearbox and a Doubly Fed Induction Generator (DFIG). Specifically, the stator windings of the generator are directly connected to the grid, while a back-to-back partial-scale static converter is installed between the rotor windings and the grid. This particular allocation of the power electronic converter is the main feature of the scheme, since it allow the rated power of the inverted to be only 30% of the DFIG rated power, although guaranteeing the regulation of the rotor frequency, the regulation of the speed, and the control of active and reactive power. However, the Type-III WTSs have also disadvantages, such as: (i) the presence of a slip ring on the rotor side for the converter connection, (ii) the need of a suitable protection system for the converter when a fault occurs and (iii) the introduction at the PCC of significant waveform distortions, due essentially to the power electronic converter, which impacts on both rotor and stator waveforms [13, 29].

More specifically, the spectral emissions of Type-III WTSs can be classified in inherent components, switching components and spectral components derived by unbalance conditions and by auxiliary loads of the system. The inherent components are related to the not-sinusoidal air gap flux and consist in low-frequency harmonics observable in both current and voltage waveforms. The corresponding frequencies can be evaluated as a function of the actual value of the induction machine slip,  $s$ , and of the fundamental frequency  $f_{fund}$  of stator voltage as:

$$f_k = |6k(1 - s) \pm 1| \cdot f_{fund} \quad \forall k \in \mathbb{N} \quad (1)$$

The switching components are the most significant components, and they are introduced by the static converter. Specifically, the PWM technique that is used for the control of the converter determines spectral components mainly at high frequency, i.e. around the switching frequency and its multiple, both on the rotor side (and therefore recalled also in the stator side) and on the grid side of the converter. As well known, the frequencies  $f_{k,m}^{PWM}$  of the spectral components due to PWM technique, in ideal operative conditions, are given by:

$$f_{k,m}^{PWM} = f_0 + [k \cdot f_{sw} \pm m \cdot f_0] \quad \forall k \in \mathbb{N}, \forall m \in \mathbb{N}_0 \quad (2)$$

where  $f_{sw}$  is the switching frequency, that could be different on the rotor and on the grid side of the converter, and  $f_0$  is: (i) on the grid side, the power system fundamental frequency ( $f_0 = f_{fund}$ ); (ii) on the rotor side, the fundamental frequency of the voltage on that side, which depends on the wind speed and on the gear ratio. The switching components introduced in the rotor side are induced in the stator of the generator, so these components are shifted in frequency at the PCC in dependence on the induction machine slip [13, 32].

When over-modulation conditions occur, also odd low-frequency components are introduced by the PWM technique [13]. The last typology of spectral components introduced at the PCC by the Type-III WTS is due to unbalanced conditions or WTS auxiliary loads (i.e., controllers and motors) [13, 32].

Finally, the fourth configuration (Fig. 2d) is identified as Type-IV wind turbine system and is a gearless WTS, characterized by either an induction or a permanent-magnet synchronous generator and a full-scale power electronic converter in cascade. This converter guarantees a self-supporting control of the active/reactive power and the decoupling between the grid and the WTS when a fault occurs, but, on the other hand, the converter cost is higher than the converter used in the Type-III WTS, since, in this configuration, the converter rated power has to be 110% of the rated power of the generator [13, 29].

Even in this configuration, the power electronic converter is the main source of spectral emissions at the PCC, but in this case less spectral components should be detected than in the Type-III wind turbine system, since there is no direct influence through the air gap of the machine. Specifically, in ideal conditions, low-frequency harmonics of order  $6k \pm 1$  could be introduced in presence of a six-pulse three-phase bridge rectifier, and therefore a ripple in the DC voltage, in input to

the inverter, could occur [33]. Voltage and current high-frequency components are introduced by the PWM at the PCC, according to eq. (2) with  $f_0 = f_{fund}$ . Also low-frequency components could be detected, when an over-modulated PWM technique is used [13, 27-28].

Other additional distortions at the PCC of a Type-IV wind turbine system can occur in unbalanced conditions or can be introduced by WTS auxiliary loads [13].

The aforesaid analysis of the waveform distortions introduced by the four typologies of WTSs includes only the primary emission of these systems. However, also secondary emissions are expected at the PCC due to background voltages [13].

### III. THE SLIDING-WINDOW MODIFIED ESPRIT METHOD

In order to acquire detailed information about the distortion levels caused by actual PVSs and WTSs at the PCC, some PQ indices have been defined in the relevant literature; the evaluation of these indices is conditional to a spectral analysis of the current or voltage waveforms.

The IEC standards recommend, for the spectral analysis, the use of Discrete Fourier Transform (DFT) over successive, rectangular time windows with a fixed duration equal to 10 cycles (12 cycles) of the fundamental period for 50-Hz (60-Hz) systems [34-35]. However, this method is affected by well-known problems, such as the spectral leakage and the fixed frequency resolution, which prevent detailed information on the single spectral components.

In the relevant literature, many spectral analysis methods have been proposed as alternative to the IEC method, in order to overcome the aforesaid problems [36-43]. Among these techniques, reference [17] presented a sliding-window modified ESPRIT method, characterized by both accurate results and reduced computational efforts.

This method is developed by observing that usually the damping factors and the frequencies of spectral components in the power system applications vary slightly versus time, so it is possible to estimate them only a few times, keeping them constant or piecewise constant along the waveform that is analyzed. In particular, the time analysis windows are divided in basis- and no basis-windows, depending on if a traditional ESPRIT algorithm (TEA) or a modified ESPRIT algorithm (MEA) is applied, respectively. In the basis-windows, including the first analysis window, the waveform is analyzed using the traditional ESPRIT model given by:

$$\hat{x}(n) = \sum_{k=1}^M A_k e^{j\psi_k} e^{(\alpha_k + j2\pi f_k)nT_s} + r(n), \quad n = 0, 1, \dots, N - 1 \quad (3)$$

where  $T_s$  is the sampling time,  $M$  is the number of exponentials,  $N$  is the number of samples in the analysis window,  $r(n)$  is the added white noise and  $A_k$ ,  $\psi_k$ ,  $f_k$ , and  $\alpha_k$  are the amplitude, the initial phase, the frequency, and the damping factor of the  $k$ th complex exponential, respectively;  $A_k$ ,  $\psi_k$ ,  $f_k$ , and  $\alpha_k$  are the unknown parameters of the model.

The unknowns are evaluated by solving two equation systems. More in detail: (i) firstly, the eigenvalues  $\hat{\lambda}_k^{BW} = e^{\alpha_k^{BW} + j2\pi f_k^{BW}}$  of the rotational matrix are computed, in order to obtain the frequencies and the damping factors; (ii) then, the solution of the equation system constituted by the theoretical definition of the correlation matrix  $R_x$  and by the matrix form of eq. (3) is searched with the aim of evaluating the amplitude and the initial phases. In these windows, also the search of the optimal values of the number  $M$  of exponentials and of the order  $N_1$  of the correlation matrix is effected; they are updated if the reconstruction error is higher than a pre-fixed threshold. In the no basis-windows, the spectral component parameters  $A_k^{BW}$ ,  $f_k^{BW}$ ,  $\psi_k^{BW}$ ,  $\alpha_k^{BW}$  obtained by the basis-window are used in the applied ESPRIT model which is:

$$\hat{x}(n) = \sum_{k=1}^M A_k e^{j\psi_k} e^{(\alpha_k^{BW} + j2\pi f_k^{BW})nT_s} + r(n) \quad (4)$$

where the only unknown parameters are the amplitudes and the initial phases of the  $M$  complex exponentials. It is clear that in these windows the computational burden is less than half of the computational burden required for a basis-window, since only the second equation system has to be solved, and the optimal  $M$  and  $N_1$  values do not have to be determined.

Note that, in order to prevent masking effects due to significant variations of frequencies, their evaluation is repeated periodically, generating a new basis-window after a certain number  $k_f$  of no basis-windows. The  $k_f$ -value depends on the particular waveform to be analyzed, and it can be changed dynamically during the analysis, based on different criteria. At each basis-windows, the frequencies and the damping factors are updated and, for the further no basis-windows, the analysis restarts with these new values.

### IV. NUMERICAL APPLICATIONS

The advanced parametric method shown in Section III was used to analyze the waveform distortions due to actual PVSs and WTSs, in order to compare the detected spectral components with the theoretically-expected components.

Several numerical experiments were effected, but for sake of conciseness, only three case studies are reported in this Section. Each of them refers to the analysis of measured current waveforms, and, in particular, the first case study deals with a current recorded at the PCC of a PVS, while, in the second and third case study, a measured current of a Type-I and Type-III wind turbine is analyzed, respectively.

The spectral analysis were performed in MATLAB environment, with programs developed and tested on a Windows PC with an Intel i7-3770 3.4 GHz and 16 GB of RAM.

#### 4.1. CASE STUDY 1

Two 1-s current waveforms were recorded at the PCC of a PVS constituted by two 10-kW, three-phase inverter without isolation transformer. The currents were measured on to the same phase of the same inverter and were taken in correspondence of two different levels of produced power: the

first measurement was taken at 8:00 AM, when a low power production was detected; the second measurement was taken at 1:00 PM, when the maximum power supplied in the day was detected. Their time trends are shown in Fig. 3a and Fig. 3b, respectively, and they clearly show different amplitudes and different levels of harmonic and interharmonic.

In both cases the sampling rate was 10 kHz, but a resampling to 20 kHz was performed in order to obtain better performances in the application of the parametric method described in Section III. The reconstruction error threshold for the spectral analysis method was chosen to be equal to  $10^{-3}$ , and the window of analysis is set to slide of 0.04 s.

The spectral analysis revealed mainly the presence of low-frequency spectral components. In fact, although some components were detected in the frequency range 5÷10 kHz, their amplitude was lower than 0.05% of the fundamental amplitude, probably as a consequence of the filter effect; then, they are not reported in the following.

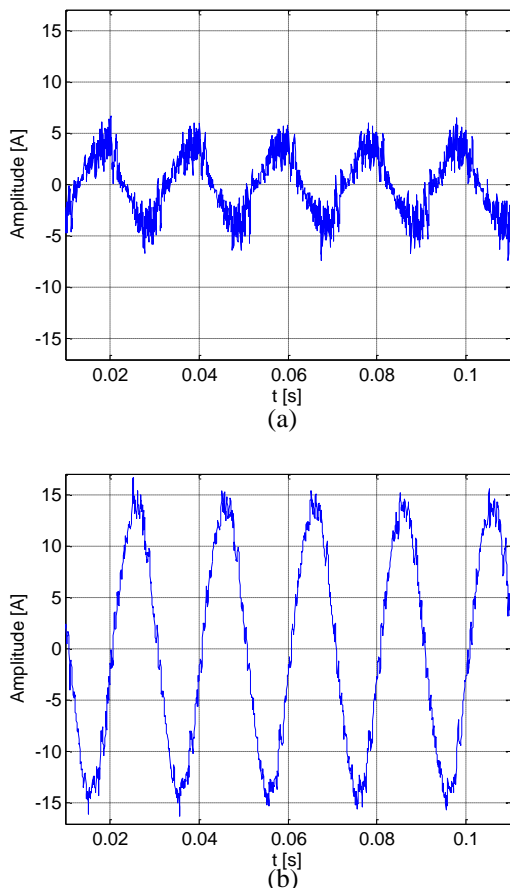


Fig. 3, Case study 1: time trend of the measured current at the PCC of the PVS (a) at the 8:00 AM and (b) at the 1:00 PM.

Fig. 4 shows the spectra obtained by the analysis in the frequency range 0÷5 kHz. Specifically, Fig. 4a shows the spectrum of the current measured at 8:00 AM and Fig. 4b shows the spectrum of the current measured at 1:00 PM. The spectra appear wide and dense in frequency, and, especially for high power production of the system, the amplitudes of both harmonic and interharmonic components have a

decreasing trend as the frequency grows. In Fig.4, the fundamental amplitudes both at 8:00 AM and at 1:00 PM are broken off for sake of clearness of the figures; they have a peak value equal to 3.72 A and 13.84 A, respectively. The amplitude scales of the figures were set to magnify all of the other spectral components, that are significantly lower than the fundamental. Coherently with the theoretical expectations, the  $THD_i$  of the two currents, evaluated up to 2 kHz, are significantly different; in fact, for the current related to a low level of power production (8:00 AM), the  $THD_i$  is about 34%, while, for the current measured at 1:00 PM, the  $THD_i$  is slightly higher than 7%. However, comparing the two spectra, it seems that globally the same components are detected, and harmonic and interharmonic amplitudes at 8:00 AM are slightly higher than those observed at 1:00 PM, especially at low-frequency, so the difference in the  $THD_i$  values is mainly due to the different fundamental amplitude of the two currents.

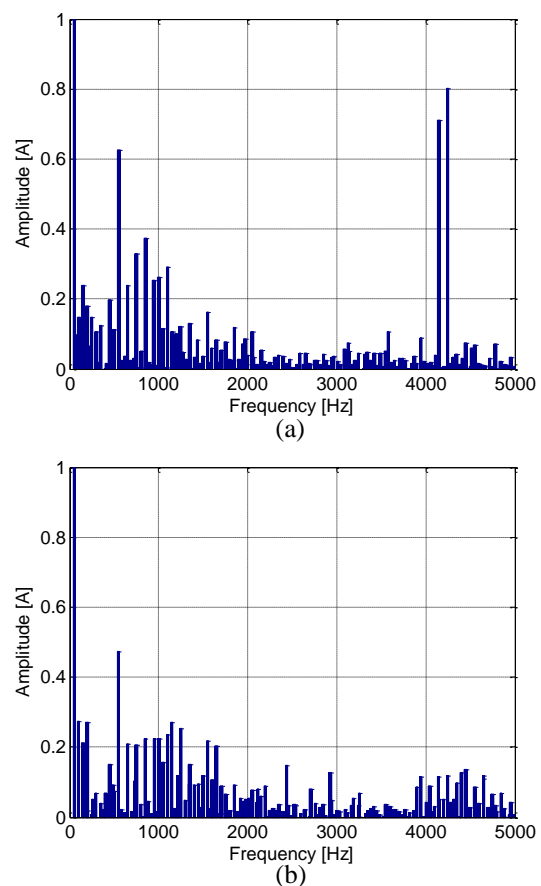


Fig. 4, Case study 1: spectra of the analyzed currents (a) at the 8:00 AM and (b) at the 1:00 PM.

Note that all of the odd and even low-frequency harmonics are detected in both the currents; an investigation on the possible origins of these components was performed. PWM over-modulation is not a suitable cause, since the amplitude modulation ratio is about 0.8. Some components could be introduced by slightly-unbalanced voltage conditions, but in this case the degree of dissymmetry is equal to 1.52%, so the main part of these spectral components probably is due to background voltages.

The presence of two high-frequency components in the sideband centered around 4200 Hz, for the 8:00 AM current, is particularly interesting. The nature of these components is typical of those due to the switching frequency of the inverters, but, since in the current at 1:00 PM their amplitudes decrease, they are probably related to a secondary emission that could be caused by voltage background. In the current at 1:00 PM, other components are detected in the sideband around 2700 Hz. These components appear to be reduced in amplitude in the current at 8:00 AM, so it is possible that are related to a primary emission introduced by the system. Since the aforesaid frequency is incompatible with the common switching frequency, in absence of other information about the system, we could hypothesize that an aliasing phenomenon occurred due to an inadequate sampling rate of the measurements.

4.2. CASE STUDY 2

A 6-s current waveform was recorded during the soft-starting of a Type-I wind turbine. The original sampling rate (2048 Hz) proved to be inadequate for the spectral analysis with the chosen parametric method, so a resampling at 10 kHz was necessary.

For the analysis, the error threshold was set to  $10^{-7}$ , and it was imposed that the window of analysis slid forward by 0.02 s versus time. In Fig. 5a and Fig.5b the time trend of few seconds of this current, and a detail of the same waveform are shown, respectively, in order to point out both its high non-stationary behavior and the typical waveform distortions.

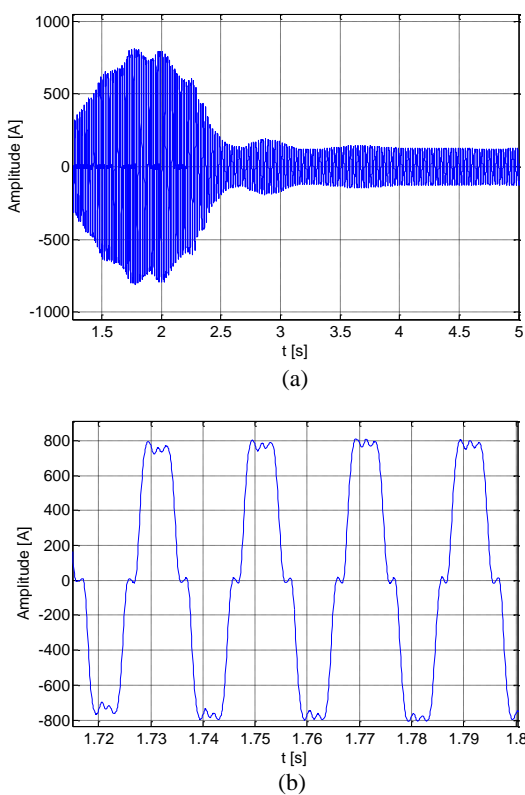


Fig. 5, Case study 2: (a) time trend of the analyzed current; (b) a detail of the same waveform

As expected from the theoretical considerations reported in Section II, the spectral analysis detected that, beyond the fundamental component, also the 3rd, 5th, 7th and 11th harmonic orders had a significant amplitude. Specifically, the time trend of the amplitudes of all of these harmonics appears to increase initially up to a maximum value, and then it decreases until their steady-state value is reached, as shown in Fig. 6, where the time trends of RMS amplitudes of the 5th, 7th and 11th harmonics are provided.

Also in this case, some high-frequency components were detected between 4 kHz and 5 kHz. However, their amplitudes are negligible, being less than 0.03% of the maximum value of the fundamental peak amplitude, that is 864.24A.

4.3. CASE STUDY 3

A 0.2-s current waveform was recorded at the PCC of a Type-III wind turbine. The original sampling rate was 12.8 kHz, so the adopted parametric method was able to detect spectral components in the range of frequency 0÷6400 Hz. The harmonic and interharmonic components appeared severely attenuated as the frequency increases, due to the effect of the filter. In particular, the amplitudes of the components above 3 kHz were lower than 0.04% of the fundamental amplitude, so these components were not dealt with. For the analysis, the error threshold was set to  $10^{-5}$ , and it was imposed that the window of analysis slid forward by 0.01 s versus time. Fig. 7 shows the time trend of the measured current; its stationarity in the time is evident, as well as the reduced waveform distortion. The fundamental component was detected at 50.038 Hz with a peak amplitude of 29.63 A. The other spectral components do not overcome the 1% of the fundamental amplitude, as shown in Fig. 8, where the spectrum obtained by the analysis is reported.

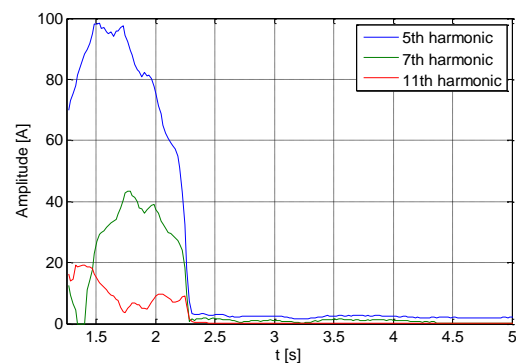


Fig. 6, Case study 2: time trend of the most significant harmonic components

For sake of clearness, the spectrum is divided in two different ranges of frequency: the behavior of the spectrum in the 0÷500 Hz range is shown in Fig. 8a, and the behavior of the spectrum in the 500÷2700 Hz range is shown in Fig. 8b. In both cases, the presence of the inherent components is evident, and they appear to be mainly “twin” interharmonics in correspondence of frequencies that are very close to those expected by applying eq. (1) with similar amplitudes.

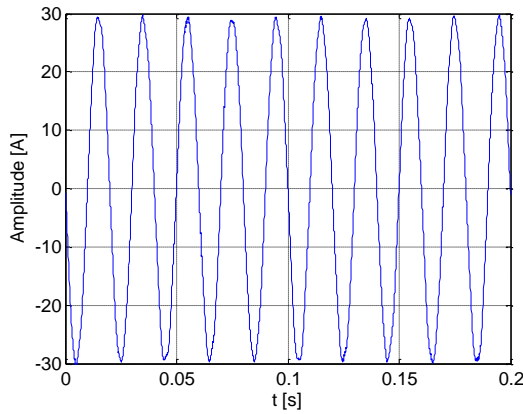


Fig. 7, Case study 3: time trend of the measured current

For example, in Fig. 8a, this behavior can be observed for the interharmonics at 284.94 Hz and at 387.21 Hz, whose amplitudes are equal to 0.28 A and 0.25 A, respectively, and were obtained by eq. (1) for  $k=1$ . Similarly, in Fig. 8b, the interharmonics expected for  $k=2$  can be detected at 620.46 Hz and at 717.27 Hz with amplitudes of 0.02 A and of 0.03 A, respectively, and so on.

The harmonics of order 2nd, 3rd, 4th, 5th and 7th also are significant, but their amplitudes are however lower than the first group of inherent components, as shown in Fig. 8a. Finally, Fig. 8b shows that in correspondence of 2.3 kHz there is another significant component, whose amplitude is about 0.24 A. This component could be due to the switching frequency of the static converter on the grid side.

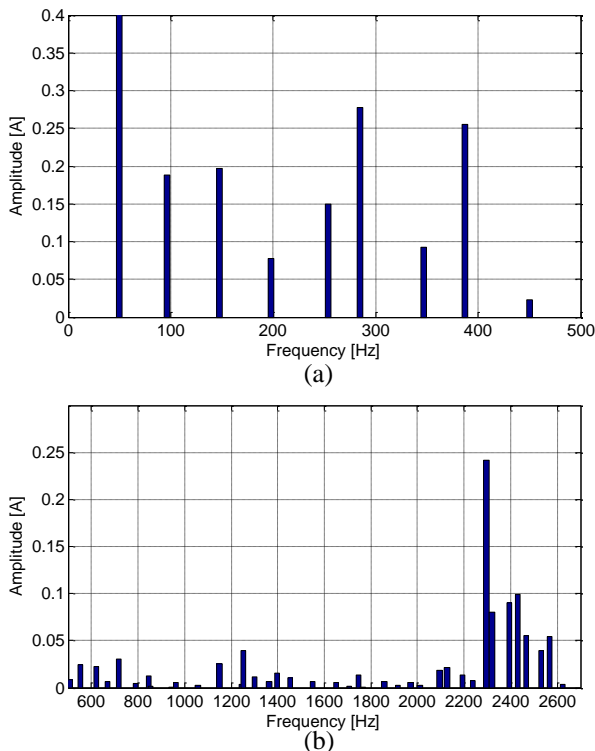


Fig. 8, Case study 3: spectrum of the analyzed current (a) in the range of frequency 0÷500 Hz and (b) in the range of frequency 500÷2700 Hz

## V. CONCLUSIONS

This paper deals with the waveform distortions caused by the most common PVSs and WTSs. For the different configurations of both systems, a distinction was made among low- and high-frequency spectral emissions, evidencing how the presence of an electronic static converter in the scheme contributes generally to introduce high-frequency disturbance components, and low-frequency spectral components only when over-modulated PWM techniques are used for the control of the converter.

The theoretical discussion was enriched by some numerical applications, where current waveforms measured at the PCC of a PVS and of two different WTS types were analyzed through a modified ESPRIT method. The results of these analyses were proved to be compatible with the theoretical expectancies.

## ACKNOWLEDGEMENT

The authors thank Prof. Guido Carpinelli for his constructive support in the realization of this work.

## REFERENCES

- [1] R.H. Lasseter. "Smart Distribution: Coupled Microgrids," *Proceedings of the IEEE*, **99**, pp.1074-1082, 2011
- [2] P. Caramia, G. Carpinelli, and P. Verde. *Power Quality Indices in Liberalized Markets*. New Jersey: Wiley-IEEE Press, 2009
- [3] F. Blaabjerg, Z. Chen, and S. Baekhoej Kjaer. "Power Electronics as Efficient Interface in Dispersed Power Generation Systems," *IEEE Trans. on Power Electronics*, **19**, pp. 1184-1194, 2004
- [4] R. Angelino, A. Bracale, G. Carpinelli, M. Mangoni, and D. Proto. "Dispersed generation units providing system ancillary services in distribution networks by a centralized control," *IET Renewable Power Generation*, **5**, pp. 311-321, 2011
- [5] F. Gronwald. "Frequency versus time domain immunity testing of smart grid components," *Adv. Radio Sci*, **12**, pp. 149-153, 2014
- [6] R.C. Variath, M. A E Andersen, O.N. Nielsen, and A. Hyldgard. "A review of module inverter topologies suitable for photovoltaic systems," *IPEC, 2010 Conference Proc.*, pp. 310-316, 2010
- [7] S. A. Papathanassiou, and M. P. Papadopoulos. "Harmonic analysis in a power system with wind generation," *IEEE Transactions on Power Delivery*, **21**, pp. 2006-2016, 2006
- [8] S.T. Tentzerakis, and S.A. Papathanassiou. "An Investigation of the Harmonic Emissions of Wind Turbines," *IEEE Transactions on Energy Conversion*, **22**, pp. 150-158, 2007
- [9] A.E. Feijoo, and J. Cidras. "Modeling of Wind Farms in the Load Flow Analysis," *IEEE Transactions on Power Systems*, **15**, 2000

- [10] J.I. Herrera, T.W. Reddoch, and J.S. Lawler. "Harmonics generated by two variable speed wind generating systems," *IEEE Transactions on Energy Conversion*, **3**, pp. 267–273, 1988
- [11] M. H. J. Bollen, and Kai Yang. "Harmonic Aspects of Wind Power Integration", *Journal on Modern Power Systems on Clean Energy*, 2013, **1**, pp. 14–21, 2013
- [12] ,” *Journal on Modern Power Systems on Clean Energy*, 2013, **1**, pp. 14–21, 2013
- [13] *Wind Turbine Generator Systems, Part 21: Measurement and Assessment of Power Quality Characteristics of Grid Connected Wind Turbines*, IEC 61400-21, 2001
- [14] L. Alfieri. "Some advanced parametric methods for assessing waveform distortion in a smart grid with renewable generation," *EURASIP Journal on Advances in Signal Processing*, **2015**, pp. 1-16, 2015
- [15] S. K. Rönnerberg, M. H. Bollen and E. O. A. Larsson. "Emission from small scale PV-installations on the low voltage grid," *Renewable Energy and Power Quality Journal (RE&PQJ)*, 2014
- [16] D. Gallo, R. Langella, A. Testa, J.C. Hernandez, I. Papic, B. Blazic, and J. Meyer. "Case studies on large PV plants: Harmonic distortion, unbalance and their effects," *Power and Energy Society General Meeting (PES)*, pp.1-5, July 21--25, 2013
- [17] M. H. Bollen and F. Hassan. *Integration of Distributed Generation in the Power System*. New Jersey: Wiley-IEEE Press, 2011.
- [18] L. Alfieri, G. Carpinelli, and A. Bracale. "New ESPRIT-based method for an efficient assessment of waveform distortions in power systems," *Electr Power Syst Res*, **122**, pp. 130–139, 2015.
- [19] R. Teodorescu, M. Liserre, and P. Rodriguez. *Grid Converters for Photovoltaic and Wind Power Systems*. New Jersey: Wiley-IEEE, 2011.
- [20] J. Zhao, Y. Wang, K. Qu, and F. Li. "Analysis and evaluation of current distortion for photovoltaic system with isolation transformer," *Renewable Power Generation, IET*, **8**, pp. 757-764, 2014
- [21] G. Chacko, and R. Scaria. "An Improved Single Phase Transformer less Inverter Topology for Cost Effective PV Systems," *International OPEN ACCESS Journal Of Modern Engineering Research*
- [22] S.K. Ronnberg, Kai Yang, M.H.J. Bollen, and A.G.de Castro. "Waveform distortion - a comparison of photovoltaic and wind power," *16th Int. Con. on Harmonics and Quality of Power*, pp. 733-737, May 25--28 May, 2014
- [23] M.J. Ortega, J.C. Hernández, and O.G. García. "Measurement and assessment of power quality characteristics for photovoltaic systems: Harmonics, flicker, unbalance, and slow voltage variations," *Electric Power Systems Research*, **96**, pp. 23-35, 2013
- [24] *EMC - Part 3-2: Limits - Limits for Harmonic Current Emissions (Equipment Input Current  $\leq 16A$  per Phase)*, IEC 61000-3-2, 2009
- [25] *EMC - Part 3-12: Limits - Limits for Harmonic Currents Produced by Equipment Connected to Public Low-Voltage Systems with Input Current  $>16A$  and  $\leq 75A$  per Phase*, IEC 61000-3-12, 2004
- [26] M. Klatt, A. Dorado, J. Meyer, P. Schegner, J. Backes, and R. Li. "Power Quality Aspects of Rural Grids with High Penetration of Microgeneration, Mainly PV-Installations," *In Proceedings of the 21st International Conference on Electricity Distribution*, Frankfurt, Germany, June 6—9, 2011
- [27] N. Mohan, W. P. Robbins, and T. M. Undeland. *Power Electronics: Converters, Applications, and Design*. New Jersey: Wiley, 1995
- [28] H. Li, and Z. Chen. "Overview of Different Wind Generator Systems and their Comparisons," *IET Ren. Pow. Gen.*, **2**, pp.123-138, 2008
- [29] E. Muljadi, N. Samaan, V. Gevorgian, Jun Li, and S. Pasupulati, "Short Circuit Current Contribution for Different Wind Turbine Generator Types," *IEEE PES General Meeting*, pp. 25-29, 2010
- [30] T. Ackermann. *Wind Power in Power Systems*. Chichester, UK: John Wiley & Sons, Ltd, 2005
- [31] *Measurement and assessment of power quality characteristics of grid connected wind turbines*, IEC 61400-21, 2008
- [32] P. Chirapongsananurak, and S. Santoso. "Harmonic analysis for fixed-speed wind turbines," *Power and Energy Society General Meeting (PES)*, pp. 1-4, July 21—25, 2013
- [33] G. L. Xie, B. H. Zhang, Y. Li, and C. X. Mao. "Harmonic Propagation and Interaction Evaluation between Small-Scale Wind Farms and Nonlinear Loads," *Energies*, **6**, pp. 3297-3322, 2013
- [34] K. Yang. *Wind-Turbine Harmonic Emissions and Propagation through A Wind Farm*. Degree: Licentiate of Engineering, Supervisor: Math H.J.Bollen, 2012
- [35] *Testing and measurement techniques - Power quality measurement methods*. IEC standard 61000-4-30, 2008
- [36] *General guide on harmonics and interharmonics measurements, for power supply systems and equipment connected thereto*. IEC standard 61000-4-7, 2009
- [37] P. Ribeiro. *Time-Varying Waveform Distortions in Power Systems*. New Jersey: John Wiley & Sons, 2009
- [38] G.W. Chang, and Cheng-I Chen. "Measurement Techniques for Stationary and Time-varying Harmonics," *IEEE Power & Energy Society General Meeting 2010*, pp. 1-5, Minneapolis, USA, July, 2010
- [39] P.M. Silveira, C. Duque, T. Baldwin, and P.F. Ribeiro. "Sliding window recursive DFT with dyadic downsampling — A new strategy for time-varying power harmonic decomposition," *IEEE Power & Energy Society General Meeting*, 2009
- [40] A. Bracale, P. Caramia, and G. Carpinelli. "Adaptive Prony Method for Waveform Distortion Detection in Power Systems," *Int. Journal of Electrical Power & Energy Systems*, **29**, 2007
- [41] I. Gu, and M. H. J. Bollen. "Estimating Interharmonics by Using Sliding-Window ESPRIT," *IEEE Trans. on Pow. Del.*, **23**, 2008
- [42] A. Bracale, G. Carpinelli, I. Y. H. Gu, and M. H.J. Bollen. "A new joint sliding-window ESPRIT and DFT scheme for waveform distortion assessment in power

- systems,” *Electric Power Systems Research*, **88**, pp. 112-120, 2012
- [43] L. Alfieri, A. Bracale, P. Caramia, and G. Carpinelli. “Waveform Distortion Assessment in Power Systems with a New Three-step Sliding-Window Method,” *13th Int. Conf. IEEEIC*, Wroclaw, Poland, May 5—8, 2013
- [44] J. Zygarlicki, M. Zygarlicka, J. Mroczka, K.J. Latawiec. “A Reduced Prony's Method in Power-Quality Analysis—Parameters Selection,” *IEEE Transactions on Power Delivery*, **25**, pp. 979-986, 2010



# Hydrogenation of carbon dioxide to synthetic natural gas: impact of catalyst bed arrangement

## 二氧化碳加氢合成天然气：催化剂床安排之影响

Andreas Martin\*, Daniel Türks, Hesham Mena, Udo Armbruster

*Leibniz Institute for Catalysis, 18059 Rostock, Germany*

*andreas.martin@catalysis.de*

Accepted for publication on 3<sup>rd</sup> December 2015

**Abstract** – Hydrogenation of carbon dioxide to synthetic natural gas (SNG) might be a future facet of energy storage solutions. This reaction can be run heterogeneously catalyzed at moderate pressure, it proceeds with high carbon dioxide conversions and extremely good SNG selectivity but it is highly exothermic. It can be operated at large scale in different reactor types but also in small units using simple tube reactors for decentralized solutions to turn excess electric power into storable SNG via intermediate hydrogen. In this paper, we describe the impact of catalyst bed arrangement on reaction heat distribution over the reactor as the basis for further simulations to receive the highest yield and productivity.

**Keywords** – carbon dioxide, synthetic natural gas, methanation, catalysis.

### I. INTRODUCTION

Till date, the energy and chemical industries bases are mainly focused on the use of crude oil, natural gas and coal, in general. Only a minor part of other resources is applied in the energy sector such as nuclear and hydroelectric power, wind, geothermal energy, solar radiation and biomass. The global chemical industries used about 750 million tons of crude oil equivalents in 2012. Two third of this amount is covered by crude oil itself, 13% stems from natural gas and only 4% from coal [1]. Remarkably, 15% belongs to biomass feedstock (e.g. oils and fats, sugars, starch, cellulose etc.). However, sustainable and “green” resources have to be fixed for future applications because the fossil resources are finite. This scenario also applies to the energy sector. Time is short and the maximum of crude oil production, so called “peak oil”, is expected soon. Therefore, our world is presently facing a feedstock change with respect to energy production and chemical industry, too [e.g. 2, 3].

One of these alternatives might be the manufacture of biogas from different biomass sources, e.g. via fermentation. In general, biogas contains carbon dioxide and methane (50-70 vol% of CH<sub>4</sub> in dependence on feed); in addition, some impurities like hydrogen, hydrogen sulfide, nitrogen, ammonia and water vapor are present. World biogas production rapidly increased in recent years. More than 14,000 biogas plants (>7,500 MW power generation) existed in Europe by the end of 2013. Germany, Austria, UK and Sweden are leading in terms of its utilization for various applications (e.g. electricity, heat or fuels). Germany is Europe's biggest biogas producer and world leader in biogas technology. Roughly 8,000 plants (in 2014) are generating 3,859 MW of power with an annual turnover of ~7.9 billion €. However, the fraction of CH<sub>4</sub> produced from fermentation of renewables has only reached 3% of the total German CH<sub>4</sub> consumption [1-3]. Beside energetic usage of the biogas methane fraction by combustion, biogas also can be seen as a future raw material for chemical syntheses. A known example of combined use of both CH<sub>4</sub> and CO<sub>2</sub> is the “dry reforming” reaction to produce syngas (CO, H<sub>2</sub>) [e.g. 4]. Another suitable option is the direct conversion of methane into formaldehyde or methanol via selective oxidation [e.g. 5, 6]. Moreover, the carbon dioxide portion might serve as feedstock for the manufacture of substitute or synthetic natural gas (SNG) by hydrogenation [e.g. 7].

At present, an increasing amount of electric power is produced from wind parks, biogas and photovoltaic plants. However, these energies are subjected to temporal fluctuation due to weather conditions. Very often wind turbines have to be switched off not to overstress the power grid. Indeed, one of the emerging tasks in future energy supply is the effective storage of electric power. An often discussed storage option for such excess electrical energy would be the generation of “green” hydrogen by water electrolysis and its temporal

storage in already available infrastructures like the gas grid, underground caverns or high pressure and liquid hydrogen tanks. But only lower amounts in single-digit percentage range might be allowed in gas grid or caverns, otherwise liquid hydrogen needs costly equipment.

The chemical conversion of such “green” hydrogen and easily available carbon dioxide to SNG is known as Sabatier reaction [8, 9]. Thereby, CO<sub>2</sub> fraction in biogas could be upgraded to SNG, significantly increasing the productivity of a biogas plant. This long-serving reaction is carried out in industry for cleaning of hydrogen from steam reforming in the presence of hydrogenation catalysts to remove CO and CO<sub>2</sub> traces [e.g. 10]. The reaction is highly exothermic and controlled by chemical equilibrium, and therefore the process is run at ca. 250-400 °C mainly over Ni-containing catalysts. It benefits from increasing pressure and is very selective toward SNG. At higher temperature, other reactions like reversed water-gas shift reaction affect the methane yield. Noble metal proportions might increase the productivity. A nice overview on applied catalyst systems is given in [11].

Interestingly, this process is suited to convert even considerable amounts of carbon dioxide, which are accessible not only from biogas plants, but also from power plants or chemical industries. This offers a large-scale chemical storage option, as “green” hydrogen is temporarily bound to carbon (CO<sub>2</sub>) and CO<sub>2</sub> can be recycled with little loss. Anyway, it will definitely not solve the global CO<sub>2</sub> problem.

Car manufacturer Audi’s new power-to-gas facility in Werlte (Lower-Saxony, Germany) [12] came into operation in mid-2013; it is a 6 MW<sub>el</sub> plant (1.5 million normal m<sup>3</sup> per annum) connected to a biogas plant. Clariant has supplied the methanation catalyst [13]. The world’s largest SNG plant went on-stream last year (1.4 billion normal m<sup>3</sup> per annum) in Yining/China with catalysts and process technology from Haldor Topsoe [14].

As mentioned above, the Sabatier reaction is highly exothermic.



However, this is not a problem in conventional application where carbon oxide traces have to be removed from gas streams by hydrogenation, but in case of selective SNG synthesis, exothermicity might cause heat transfer problems and even thermal runaway of the reactor. As a first consequence, the chemical equilibrium may be shifted away from optimum conditions. Own experiments have already shown the formation of hot-spots up to 15 K at the top of the catalyst bed [7]. Kienberger and Karl reported on the conversion of a CO/CO<sub>2</sub> and H<sub>2</sub> feed stemming from biomass gasification showing a reaction temperature in the hot-spot zone of 460 °C and a gas outlet temperature of 270 °C [15]. Therefore, different reactor concepts are in operation such as cascades of fixed bed reactors with limited conversion, wall-cooled fixed bed reactors, fluidized bed reactors or slurry bubble reactors [16]. Brooks et al. recently offered a concept of SNG synthesis using microchannel reactors to effectively

remove generated heat from the reactor [17]. Anyway, hot-spots may also lead to catalyst or reactor material damage and have to be avoided. Therefore, the aim of the present work was directed to collect data on heat distribution over the catalyst bed of a tube reactor at greatest possible SNG productivity for further simulation of catalyst bed arrangement.

## II. REACTOR CONCEPT AND CATALYST

The catalytic tests were carried out with a lab set-up containing several mass flow controllers to meter feed gases, a suitable tube reactor, and a pressure transducer to measure reaction pressure, an automated pressure release valve and an on line-gas chromatograph unit for quick analysis of the feed and product stream. Details can be found elsewhere [7]. Two different stainless steel tube reactors (a) L = 276 mm, ID = 7.6 mm, V = 12.5 cm<sup>3</sup> and (b) L = 1000 mm, ID = 24.8 mm, V = 483 cm<sup>3</sup>) with heating jacket (electrical heater and oil bath, respectively) were used. Both the reactors contain a guiding tube for a moveable thermocouple to stepwise record the catalyst bed temperature. Most of the runs reported here were carried out under the following conditions: T = 250-400 °C (set temperature), p = 10 bar, GHSV = 6000-12000 h<sup>-1</sup> (referred to standard reference conditions), CO<sub>2</sub>: H<sub>2</sub> = 1: 4. In addition, nitrogen (10 vol%) was always fed as internal standard to evaluate volume contraction.

Carbon dioxide conversion (X<sub>CO<sub>2</sub></sub>) and methane (S<sub>CH<sub>4</sub></sub>) selectivity (S<sub>CH<sub>4</sub></sub>) were determined from mole streams (n) and number of carbon atoms (z) as follows:

$$X_{\text{CO}_2} = \frac{\dot{n}_{\text{CO}_2(\text{in})} - \dot{n}_{\text{CO}_2(\text{out})}}{\dot{n}_{\text{CO}_2(\text{in})}} \times 100 \%$$

$$S_{\text{CH}_4} = \frac{\dot{n}_{\text{CH}_4}}{\dot{n}_{\text{CO}_2(\text{in})} - \dot{n}_{\text{CO}_2(\text{out})}} \times \frac{z_{\text{CH}_4}}{z_{\text{CO}_2}} \times 100 \%$$

First tests on temperature and pressure dependency were mainly carried out over a homemade 5 wt% Ni/ZrO<sub>2</sub> catalyst [7, 18]. An industrially available Ni-containing catalyst (18 wt% Ni on alumina (original size: 2.5×3-5 mm extrudates), denoted as 18Ni) was used for all catalytic runs with respect to temperature profile recording. The catalyst particles were crushed and sieved, and the fraction of 500-800 μm was used for all runs. Quartz split of the same size was used for catalyst dilution. Before catalytic tests, the catalyst was in-situ activated in hydrogen.

## III. CATALYST TEST RUNS

Previous studies using monometallic Ni-, Ru and bimetallic NiRu-containing catalysts in a larger temperature and pressure

window have shown that the best results with respect to carbon dioxide conversion and SNG selectivity were received at 10 bar and 325-350 °C. In particular, an increased reaction pressure is beneficial to suppress CO and ethane formation. Observed carbon dioxide conversion always is close to the thermodynamic equilibrium [cf. 7, 18] and SNG selectivity is above 99.9%. There are two different mechanistic routes under discussion: i) the direct hydrogenation of CO<sub>2</sub> to methane without the formation of CO as intermediate and ii) the conversion of CO<sub>2</sub> to CO (reverse water gas shift reaction), followed by a methanation reaction according to the mechanism as of CO methanation [e.g. 19, 20]. CO forms an adsorbed carbon species (C<sub>a</sub>) on the catalyst surface and is subsequently hydrogenated to methane by surface hydrogen [e.g. 19, 20]. In other words, the methanation mechanism might be characterized by carbon formation and carbon methanation. However, adsorbed CO may react at low temperatures to hydrocarbons via the Fischer-Tropsch reaction (conversion of CO and H<sub>2</sub>) [e.g. 21]. Indeed, our previous runs always revealed some ethane formation (<1%) at temperatures up to 325 °C [7]. However, ethane might also be formed at higher temperatures but it is easily converted to methane in surplus of hydrogen by hydrogenolysis [22]. Table 1 gives a short summary on the results with 5 wt% Ni/ZrO<sub>2</sub> catalyst received so far.

TABLE 1, CARBON DIOXIDE CONVERSION AND SNG SELECTIVITY IN 300-400 °C TEMPERATURE RANGE AT DIFFERENT REACTION PRESSURE

T (°C)	300	325	350	375	400
X <sub>CO2</sub> <sup>a</sup>	98.5	97.7	96.5	95.5	94.0
X <sub>CO2</sub> <sup>b</sup>	19.5	38.5	54.3	66.0	71.1
X <sub>CO2</sub> <sup>c</sup>	96.7	96.8	95.9	94.6	93.2
S <sub>SNG</sub> <sup>b</sup>	99.0	99.5	99.6	99.2	98.9
S <sub>SNG</sub> <sup>c</sup>	99.8	99.9	100	99.9	99.9

5wt% Ni/ZrO<sub>2</sub> catalyst, GHSV = 6000 h<sup>-1</sup>, CO<sub>2</sub>: H<sub>2</sub>: N<sub>2</sub> = 1: 4: 5, <sup>a</sup> CO<sub>2</sub> equilibrium conversion (at 1 bar), <sup>b</sup> CO<sub>2</sub> conversion and SNG selectivity at 1 bar, <sup>c</sup> CO<sub>2</sub> conversion and SNG selectivity at 10 bar

As already mentioned, catalytic test runs at higher SNG productivity due to increased space velocity and reduced inert gas proportion and/or higher catalyst proportion showed pronounced hot-spots in the topmost part of the catalyst bed. As a crucial requirement for up-scaling trials, knowledge on prevention of hot-spot at high catalyst load is indispensable. Therefore, several tests on the arrangement of the catalyst bed at increased space velocity as well as decreased inert gas dilution (10 vol% N<sub>2</sub>) were carried out using an industrially available catalyst.

#### IV. TEMPERATURE PROFILES

Figure 1 schematically depicts the used lab tube reactor and the position of quartz split layers above and below the catalyst bed each separated by quartz wool. The right-hand scale (in cm) shows the length of the guiding tube for a thermocouple which allows temperature measurement along the catalytic bed. Length data in the figures below refer to those given here.

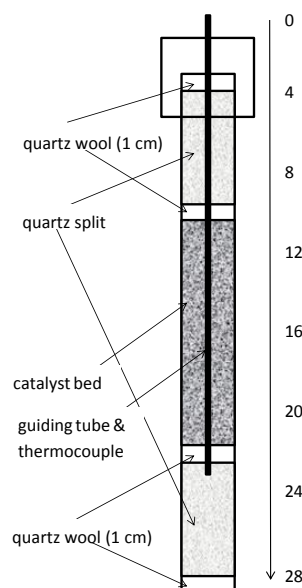


Fig.1, Schematic image of the used lab reactor and arrangement of catalyst bed (right-hand numbers are in cm).

First tests were carried out keeping the GHSV constant (ca. 6000 h<sup>-1</sup>) while the amount of catalyst and feed gas were increased proportionally in order to get a higher total SNG yield. The catalyst bed consisted of a 5 ml grain mixture containing 1 ml (run A), 2.5 ml (run B) and 4 ml (run C) of 18Ni catalyst diluted with quartz, i.e. 4 ml (A), 2.5 ml (B) and 1 ml (C). The feed gas flow was equivalently increased to keep GHSV constant: 6 l/h (A), 15 l/h (B) and 26.4 l/h (C). Highest SNG yields were observed at 325 °C (A), 300 °C (B) and 290 °C (C) set point temperature, however, one can see that hot-spot temperatures are significantly increased, i.e. they reached 325 °C, 336 °C and 358 °C, respectively. Higher set point temperatures resulted in decreasing X<sub>CO2</sub> due to equilibrium restrictions, in particular for runs A and B, however, selectivity to SNG was quite stable reaching values >99.9%. Data for run C were only be collected up to 290 °C because the hot-spot climbed up to >70 K. Table 2 summarizes these data.

TABLE 2, CARBON DIOXIDE CONVERSION AND SELECTIVITY TO SNG DURING TEST RUNS WITH DECREASING CATALYST DILUTION

T (°C)	270	280	290	300	325	350	375
A X <sub>CO2</sub>				96.5	96.9	96.1	95.1
A S <sub>SNG</sub>				99.9	99.9	99.9	99.9
B X <sub>CO2</sub>				97.3	96.8	96.5	95.4
B S <sub>SNG</sub>				99.9	99.9	99.9	99.9
C X <sub>CO2</sub>	96.5	96.7	97.4				
C S <sub>SNG</sub>	99.9	99.9	99.9				
A hot-spot				300	325	351	378
B hot-spot				336	361	384	406
C hot-spot	334	347	358				

GHSV = ca. 6000 h<sup>-1</sup>, CO<sub>2</sub>: H<sub>2</sub>: N<sub>2</sub> = 1.8: 7.2: 1, run A: cat: quartz = 1: 4, 6 l/h feed, run B: cat: quartz = 1: 1, 15 l/h feed, run C: cat: quartz = 4: 1, 26.4 l/h feed, catalyst: 18Ni

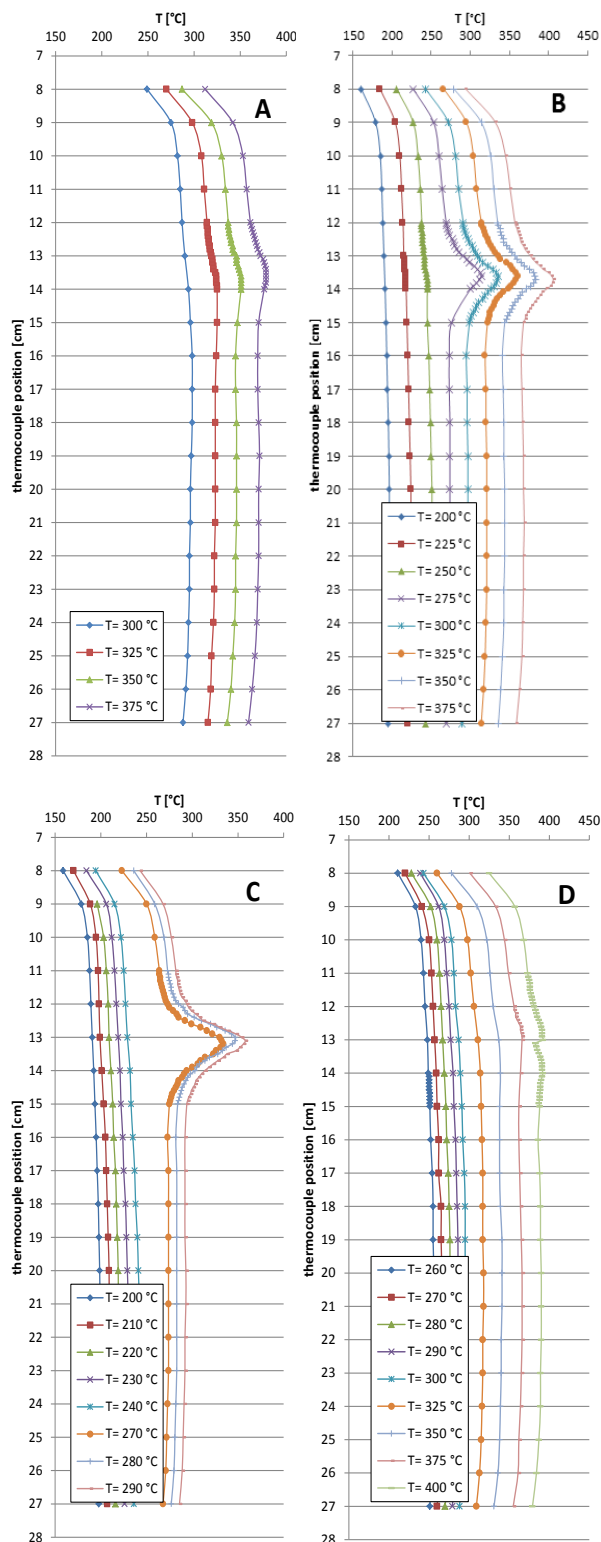


Fig.2, Temperature profiles of carbon dioxide hydrogenation runs (CO<sub>2</sub>: H<sub>2</sub>: N<sub>2</sub> = 1.8: 7.2: 1; run A: cat (1 ml): quartz = 1: 4, 6 l/h feed, 6000 h<sup>-1</sup>; run B: cat (2.5 ml): quartz = 1: 1, 15 l/h feed, , 6000 h<sup>-1</sup>; run C: cat (4 ml): quartz = 4: 1, 26.4 l/h feed, 6000 h<sup>-1</sup>; run D: cat (0.5 ml): quartz = 1: 9, 6 l/h feed, 12000 h<sup>-1</sup>; catalyst: 18Ni).

The SNG productivity grew from 1.1 l<sub>SNG</sub>/h (A) and 2.6 l<sub>SNG</sub>/h (B) to 4.6 l<sub>SNG</sub>/h (C) by increasing catalyst amount at constant space velocity, but a significantly elevated hot-spot temperature was the consequence. Therefore, the conversions were comparable at even less set point temperatures because the reaction temperatures in the hot-spot region were similar. Figure 2 shows the related temperature profiles and it is clear that the hot-spot appearance is very narrow but significant. Taking these results into account, further catalyst dilution combined with increased space velocity should lead to raised productivity at more equal temperature distribution over the whole bed.

Therefore, a further test (run E) with increased dilution of catalyst: diluent = 1: 9, i.e. 0.5 ml catalyst at increased GHSV (12000 h<sup>-1</sup>) was carried out. It revealed similar carbon dioxide conversion and selectivity to SNG, but highest X<sub>CO<sub>2</sub></sub> = 96.6% and S<sub>SNG</sub> = 99.9% were observed at 350 °C. The SNG productivity in this run was close to 2.1 l<sub>SNG</sub>/h. Interestingly, more or less no distinct hot-spot was observed as shown below (see Fig. 2). This illustrates the beneficial effect of improved temperature control on the chemical equilibrium.

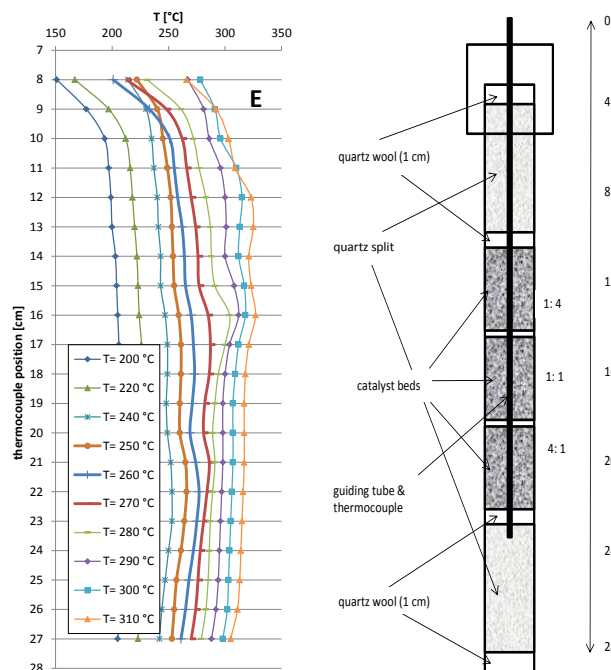


Fig.3, Temperature profile of carbon dioxide hydrogenation over structured catalyst bed (CO<sub>2</sub>: H<sub>2</sub>: N<sub>2</sub> = 1.8: 7.2: 1, GHSV = ca. 6000 h<sup>-1</sup>, 13.5 l/h feed, three catalyst zones (1.7 ml each) catalyst: quartz split diluent ratio was varied top-down from 1: 4, 1: 1 to 4: 1, catalyst: 18Ni).

As a consequence of these first test runs, the diluted catalyst bed was divided into three parts of ca. 1.7 ml each (again 5 ml in total) as shown in Figure 3. The catalyst: quartz diluent ratio was varied top-down from 1: 4 to 1: 1 and 4: 1. The three zones were separated by small quartz wool layers of ca. 5 mm. In total, a catalyst: diluent ratio of 1: 1 (as in run B) was applied

but the above described structure of the bed should lead to altered hot-spot behavior. The hydrogenation run E was carried out at 6000 h<sup>-1</sup> and 13.5 l/h feed gas (CO<sub>2</sub>: H<sub>2</sub>: N<sub>2</sub> = 1.8: 7.2: 1). A carbon dioxide conversion close to equilibrium was reached at ca. 300-310 °C set point temperature, i.e. X<sub>CO<sub>2</sub></sub> = 97.5%. The reaction temperatures in the first two beds reached 318 °C and 325 °C, respectively. This means a hot-spot of 8 and 15 K, respectively, is observed at a set point temperature of 310 °C. The SNG productivity amounted to 2.4 l<sub>SNG</sub>/h, i.e. the same value was obtained as seen for run B but hot-spot behavior dramatically changed and overall reaction temperature decreased significantly.

Based on these results further optimization aiming at increasing SNG productivity is on the way. In addition, first test runs were carried out using the large lab reactor (as a start, catalyst volume was ca. 15 ml separated in the same way to the above described run E but using four catalyst zones). The results show that a larger tube reactor can be operated at similar conditions up to space velocities of about 40000 h<sup>-1</sup>. SNG productivity was increased to 50 l/h that relates to an electrical power of 500 W. Such tubes might be incorporated in a multitube reactor to further increase of productivity.

#### IV. CONCLUSION

SNG synthesis was carried out with a commercially available Ni-containing catalyst. The catalyst dilution impact was studied to avoid hot-spot formation and damage of catalyst or reactor. The results have shown that most of the heat of reaction is produced in the topmost 10% of the catalyst bed at the feed inlet. The resulting hot-spot can be significantly suppressed by catalyst bed dilution and additionally by structuring the bed without changing overall catalyst mass. Thus, the reactor can be operated at higher load resulting in higher productivity. Catalyst dilution at the feed inlet should be very high and decrease in top-down direction.

#### Acknowledgments

The authors would like to thank the Federal State of Mecklenburg-Western Pomerania and the EU Regional Fund (EFRE) for funding (Project V-630-S-152-2012/141).

#### REFERENCES

- J. Fabri and W. Falter, „Zeit für einen Rohstoffwandel?“ *Nachrichten aus der Chemiewirtschaft*, pp. 19-22, April 2013.
- G.A. Olah, A. Goepfert, and G.K. Surya Prakash, *Beyond Oil and Gas: The Methanol Economy*. Weinheim: Wiley-VCH, 2009.
- M.J. Climent, A. Corma, and S. Iborra, “Conversion of biomass platform molecules into fuel additives and liquid hydrocarbon fuels”, *Green Chem.*, **16**, pp. 516-547, 2014.
- A. Wahyu Budiman, S.-H. Song, T.-S. Chang, C.-H. Shin, and M.-J. Choi, “Dry Reforming of Methane Over Cobalt Catalysts: A Literature Review of Catalyst Development”, *Catal. Surv. Asia*, **16**, pp. 183-197, 2012.
- H. Berndt, A. Martin, A. Brückner, E. Schreier, D. Müller, H. Kosslick, G.-U. Wolf, and B. Lücke, “Structure and Catalytic Properties of VO<sub>x</sub>/MCM Materials for the Partial Oxidation of Methane to Formaldehyde”, *J. Catal.*, **191**, pp. 384-400, 2000.
- C. Pirovano, E. Schönborn, S. Wohlrab, N. Kalevaru, and A. Martin, “On the performance of porous silica supported VO<sub>x</sub> catalysts in the selective oxidation of methane”, *Catal. Today*, **192**, pp. 20-27, 2012.
- F. Lange, U. Armbruster, and A. Martin, “Heterogeneously-catalyzed hydrogenation of carbon dioxide to methane over RuNi-bimetallic catalysts”, *Energy Technol.*, **3**, pp. 55-62, 2015.
- P. Sabatier and J.B. Senderens, “Nouvelles synthèses du méthane”, *C.R. Acad. Sci.*, **134**, pp. 514-516, 1902.
- P. Sabatier and J.B. Senderens, “Hydrogénation directe des oxydes du carbone en présence de divers métaux divisés”, *C.R. Acad. Sci.*, **134**, pp. 689-691, 1902.
- J.K. Nørskov, T. Bligaard, B. Hvolbæk, F. Abild-Pedersen, I. Chorkendorff, and C.H. Christensen, “The nature of the active site in heterogeneous metal catalysis”, *Chem. Soc. Rev.*, **37**, pp. 2163-2171, 2008.
- G. Garbarino, P. Riani, L. Magistri, and G. Busca, “A study of the methanation of carbon dioxide on Ni/Al<sub>2</sub>O<sub>3</sub> catalysts at atmospheric pressure”, *Int. J. Hydrogen Energy*, **39**, pp. 11557-11565, 2014.
- [http://www.audi.de/de/brand/de/vorsprung\\_durch\\_technik/content/2013/08/energiewende-im-tank.html](http://www.audi.de/de/brand/de/vorsprung_durch_technik/content/2013/08/energiewende-im-tank.html)
- <http://www.chemicals-technology.com/news/news-clarient-catalyst-audi-german-methanation-plant>
- <http://www.topsoe.com/Press/News/2013/281013.aspx>.
- T. Kienberger and J. Karl, *Substitute natural gas (SNG) – Stand der Technik, theoretische Grundlagen, Forschung am Institut für Wärmetechnik*, 11. Symposium Energieinnovation, 10.-12.02.2010, Graz, Austria
- <http://www.netl.doe.gov/research/coal/energy-systems/gasification/gasifipedia/coal-to-sng>
- K.P. Brooks, J. Hu, H. Zhu, and R.J. Kee, “Methanation of carbon dioxide by hydrogen reduction using the Sabatier process in microchannel reactors”, *Chem. Eng. Sci.*, **62**, pp. 1161-1170, 2007.
- M. Schoder, U. Armbruster, and A. Martin, “Heterogen-katalysierte Hydrierung von CO<sub>2</sub> zu Methan unter erhöhten Drücken“, *Chem. Ing. Tech.*, **85**, pp. 344-352, 2013.
- D.E. Peebles, D.W. Goodman, and J.M. White, “Methanation of carbon dioxide on nickel(100) and the effects of surface modifiers”, *J. Phys. Chem.*, **27**, pp. 4378-4387, 1983.
- W. Wang and J. Gong, “Methanation of carbon dioxide: an overview”, *Front. Chem. Sci. Eng.*, **5**, pp. 2-10, 2011.
- G.P. van der Laan and A.A.C.M. Beenackers, “Kinetics and Selectivity of the Fischer-Tropsch Synthesis: A Literature Review”, *Catal. Rev.-Sci. Eng.*, **41**, pp. 255-318, 1999.

- 22 J. Yang, W. Ma, D. Chen, A. Holmen, and B.H. Davis,  
“Fischer-Tropsch synthesis: A review of the effect of CO  
conversion on methane selectivity” *Appl. Catal. A:  
General*, **470**, pp. 250-260, 2014.



# The trend of ICT-based renewable energy in South Korea with a focus on cases of application of micro grids

## 侧重于韩国微电网中应用案例的基于信息通信技术之可再生能源趋势

Suhyeon Han<sup>1\*</sup>, Eunjin Jun<sup>1</sup>, Yuri Yoon<sup>1</sup>, Chulho Park<sup>1</sup>

<sup>1</sup>Future Strategy Division, Green Technology Center, Seoul 100-705, South Korea

[sue@gtck.re.kr](mailto:sue@gtck.re.kr)

Accepted for publication on 16 October 2015

*Abstract* – Although the need and demand for switching to renewable energy continue to increase, adoption of renewable energy is difficult owing to disadvantages such as unstable power supply and a rather low efficiency. In this study, a new business model was examined to overcome such disadvantages through Korea's renewable energy policy and cases analysis. The future industrial application of renewable energy depends on an ICT-combined convergence and compound power system, rather than on regular energy source support. Hence, demand response systems along with energy storage systems (ESSs) and energy management systems (EMSs) would be more emphasized for the efficient use of energy.

*Keywords*— Green energy, Renewable energy policy, Energy policy, Smart grid, ESS, EMS, ICT

### I. INTRODUCTION

Various policies and systems for responding to climate changes and energy resource depletion have been enhanced upon worldwide.

South Korea has declared “Low Carbon Green Growth” as its national vision and has put its efforts into establishing a legal and systematic foundation for the vision through the Five-Year Plan for Green Growth [1], the Framework Act on Green Growth [2], the Presidential Committee on Green Growth and executing emissions trading.

Furthermore, Korea succeeded in internationally capitalizing a green brand and achieved fruitful results, including the launch of an international institute, Global Green Growth Institute (GGGI), and successfully invited the Green Climate Fund (GCF) to Korea. In particular, with the

investment principle that 2% of the GDP is invested in green technologies, Korea took initiatives to invest in such technologies and improved its level of technologies by encouraging investment in research and development (R&D) on core green technologies.

President Park Geun-hye attended the 22<sup>nd</sup> World Energy Congress 2013, Daegu, Korea and announced her plans: “Korea will reduce energy consumption by utilizing information and communication technologies (ICT), such as energy storage systems (ESSs) and energy management systems (EMSs), and build a trading system with which the saved energy can be traded in the Korea Power Exchange”; these plans will show the way to resolving the world energy trilemma that Korea and the world are facing and will contribute to the world energy market.

From these viewpoints, the main aim of this paper is to investigate the problems that renewable energy faces and efforts to overcome these problems, then review the policies and a business model related to Korea's renewable energy.

### II. TRENDS IN RENEWABLE ENERGY

The need and demand for switching from fossil fuel to CO<sub>2</sub> reducing renewable energy continue to increase coping with climate changes.

Even in this global economic crisis, R&D investments for technological development of renewable energy and in particular, the government R&D investments continues to increase; as a result, renewable energy technologies have advanced.

However, there still remains various constraints.

- 1) High developmental unit cost compared to that of the existing fossil fuels, owing to the high initial investment costs, hinders the commercialization of renewable energy.
- 2) Moreover, the installation of renewable energy faces certain constraints (the quality of wind, the amount of sunlight, etc.), and even in the areas where the installation is practical, it conflicts with residents, making installations difficult. For example, residents express an extreme opposition because fishing is impossible where a marine wind power plant is built. With regard to biogas plants, residents consider it an unpleasant facility because the plant is based on livestock and food wastes.
- 3) The unstable supply of natural energy resources such as sunlight and wind, lowers the utilization rates of renewable energy facilities, thereby interfering with its commercialization and industrialization.
- 4) The industrial characteristic of renewable energy is of great importance in the installation, maintenance, and repair; in addition, the renewable energy industry also experiences the lack of the service.

While the necessity of the industrial development of renewable energy is recognized, the implementation of industrial development is difficult because of the above problems.

To overcome the barriers in the use of renewable energy, for example, unstable power supply and low efficiency, there is a need for the convergent use of various energy sources, thus creating a new business model.

Without governmental support, after all, the grid parity of renewable energy is very challenging; therefore, for invigorating renewable energy, a powerful drive led by the government is essential more than anything else from the viewpoint of policies and systems.

### III. RENEWABLE ENERGY POLICY IN KOREA

Since the declaration of its vision on green growth, Korea has established Five-Year Plan for Green Growth (July 2009) as a national strategy and action plan for the purpose of increasing the effectiveness of the policy. Korea has proposed national mid-long term emissions reduction targets and introduced an emission-trading system, vehicle emissions standards, etc.

Furthermore, Korea also legislated the Framework Act on Low Carbon Green Growth[2] and developed 27 core green technologies through R&D measures and strategies for commercializing the core green technologies[3] (May 2009).

<sup>1</sup> Ministry of Trade, Industry and Energy (MOTIE): A central administrative body in Korea; it governs affairs related to commerce, trade, industry, trade, trade negotiation

Fundamental studies were encouraged on these 27 core green technologies by allocating aggressive R&D budgets.

In recent years, with the establishment of “developmental strategies for new energy industries and core technologies in response to climate changes,” Korea announced its plans to invest 430 billion KRW (\$400 million) in the development of core technologies for coping with climate changes and that by 2020, the current technology level of 81% compared to those of advanced countries, will be increased to 93%.

As shown in <Figure 1>, in 2013, the total national R&D investment amount was 16 trillion KRW; the amount invested in green technologies was 3 trillion KRW (17.9%) and that in the 27 core green technologies was 2.3 trillion KRW, which makes up 76.2% of the entire R&D investment amount in green technologies. For the last six years, the average annual increase rate of the R&D investment in green technologies was 15.8%, which is higher than that of the national R&D investment (9.0%).[4]

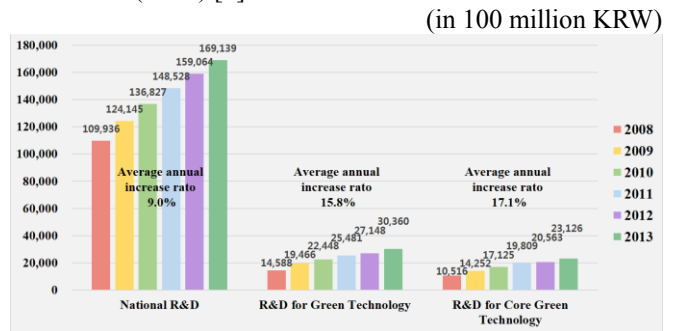


Fig.1, Green Technology R&D Expenditure from 2008 to 2013

The plans that are directly related to renewable energy are as follows:

#### 3.1. The Fourth Master Plan on Renewable Energy (2014-2035, MOTIE<sup>1</sup>) [5]

This plan suggested to increase the supply target for renewable energy over 11% by 2035. It is aiming for the creation of a renewable energy market to enable shifting the current government-led actions to a private-government partnership, and achieving sustainable growth by expanding to the international markets.

With regard to the outlook of the target per energy source, current focus on waste energy will be shifted to solar and wind. In addition, the renewable energy market will be expanded from electric energy including hydro/thermal energies by enforcing the Renewable Fuel Standard (RFS) and the Renewable Heat Obligation (RHO).

For sub-tasks, in addition, eco-friendly technologies are

and general management, mediation on trade negotiation, foreign investments, the R&D policies of industrial technology, and energy and underground resources.

applied to existing unwanted facilities including incineration plants and landfills for energy supply, and a project demonstrating an “eco-friendly energy town” will be revealed to provide benefits to the residents. Also, the island where has been 100% diesel-power system will be provided with self-sufficient micro grid system.

3.2. The Second National Master Plan for Energy (2014.1 MOTIE) [6]

As energy policies are complicated and conflicts among interested parties become sharp, private sector-led participation is essential in establishing a policy. This plan was the first open-process national plan that wholly reflected the recommendations of the private working group.

Its main points include, as shown in <Figure 2>, a shift from the current supply-managing policy to a demand-managing policy; adjustments to energy tax rates with a goal of cutting the power demand to 15% by 2035; system improvement on electricity rates; and building an ICT demand management system.

In addition, with the goal of supplying at least 15% of energy through a decentralized generation by 2035 instead of centralized generation by utilizing fossil fuels, its energy types will be diversified into renewable energy, home generators, and so on. Then, small- and mid-size enterprises will have increasing opportunities to participate in the power generation market.

In other words, this plan entails an operational shift from supplier-oriented facility to user-participating facility.

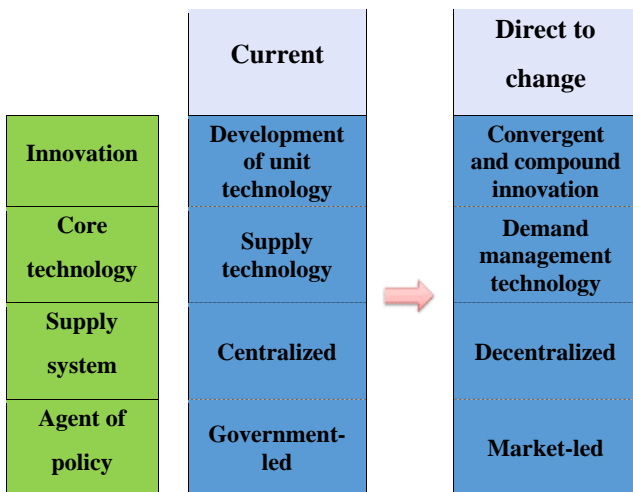


Fig.2, Directions of changes on the energy technology paradigm

3.3. The Third Energy Technology Development Plan (2014-2023) [7]

The Energy Technology Development Plan is the highest level technology development plan that covers the National Master Plan for Energy, the use of related energy, the development of renewable technology, emissions reduction, etc.

With the policy goals such as strengthening the competence of the energy industry, it was proposed to respond to climate changes through innovation and enhance the productivity of technology development, as shown in <Figure 3>, through a technology development program “Energy Innovation Architecture 2025” and core promotional strategies.

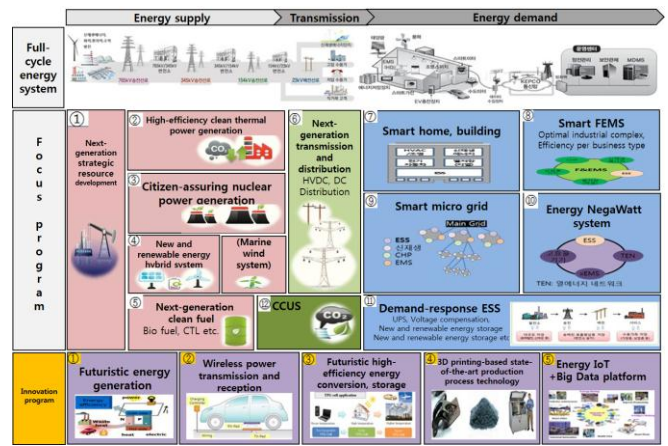


Fig.3, Concept of the program, Energy Innovation Architecture 2025

With regard to the energy supply technology part of the sub-programs, there is a renewable energy hybrid system combined with a compound generation and storage facility to provide optimal solutions that are suitable for various conditions and geographical characteristics, and this system will be applied in domestic island areas.

With regard to the energy demand management technology, the program offers a solution for an operating system solution that combines and manages decentralized resources. It also loads, connects the solution to the power network, and builds an independent operation system—a smart micro grid.

Furthermore, based on information and communications technology (ICT), the main focus of the energy NegaWatt system technology will be on the development of the energy solution services to secure the stability of energy demand and supply through combining energy sources, including ESSs, EMS, TENs (thermal energy networks), and decentralized development resource.

IV. CASE

For activating renewable energy industry, Korean government puts extra efforts to create a foundation based on ICT convergence for shared growth among energy sources, instead of supporting sources per energy. The government is seeking and generating a business model based on the foundation.

A “micro grid (MG) system” is an independent decentralized small-scale power supply system, unlike the existing wide-area power supply system. This system generates, stores, and supplies power throughout the day to

areas where power supply is constrained by using renewable energy facilities.

This concept is considered to be a rather new technology which IT is employed to store generated electric energy when the demand is low and to supply it when the demand is high.

In other words, it is an eco-friendly power system that converges and compounds various renewable energy generation sources and energy storage systems.

Now, among the proven projects, a “self-sufficient micro grid demonstration project” and the case of a building an “energy independent island” will be examined.

#### 4.1. Gasado’s self-sufficient micro grid demonstration project

Gasado is a small Korean southwestern island located in Jeollanam-do. It has a population of 303 in 165 households. This island had been 100% diesel-power dependent, but with the completion of four wind power plants and eight solar power plants along with a 3MWh ESS in 2014, its power capacity has been supplemented with 320 kW of solar power and 400 kW of wind power.

This small island suffered from chronic power shortage due to its existing diesel power plants capacity of only 300 kW; it was transformed into a state-of-the-art energy village by conversion of its power supply into hybrid power supply with a combination of wind, solar power plants and an ESS.

Some problems encountered with the project have been addressed through an optimal combination of decentralized powers with a 100% renewable energy site designing. As a result, problems such as high-capacity power transmission and distribution facilities, high costs of power transmission due to the existing long-distance power supply and the increase in power losses could be addressed.

Hence, this project is considered to have maximized the efficient use of energy through energy storage systems (ESSs), energy management systems (EMSs), demand responses (DRs), and etc., in addition to resolving the problem of unstable power generation of new and renewable energy.

#### 4.2. Ulleungdo, an eco-friendly energy independent island

Against the background of the technological development with regard to the renewable energy power sources being proved by the results achieved in Gapado of Jeju and Gasado of Jeollanam-do, the eco-friendly energy independent island plan on Ulleungdo was realized.

For the first time in Asia, Ulleungdo joined ISLENET<sup>2</sup> (2011) and emerged on the international stage as a green island.

Even though Ulleungdo has the largest power system among land power systems and independent island areas, most of its power generation capacity of 13,000 kW is derived from the thermal power plants that use diesel power generators.

According to <Figure 4>, during the first stage (2015–2017) of the project, 30% of the current diesel-oriented power generation will be substituted with an ICT(ESS+EMS)-combined eco-friendly energy supply by giving up one diesel power plant a year. There are plans to build facilities for hydro-electric power (0.696 MW), solar power (1 MW), wind power (8 MW) and a 21 MWh ESS. In the second stage, facilities for geothermal power (4 MW) and fuel batteries (23 MW) will be added, expanding to a total of 36.5 MWh ESS facilities.

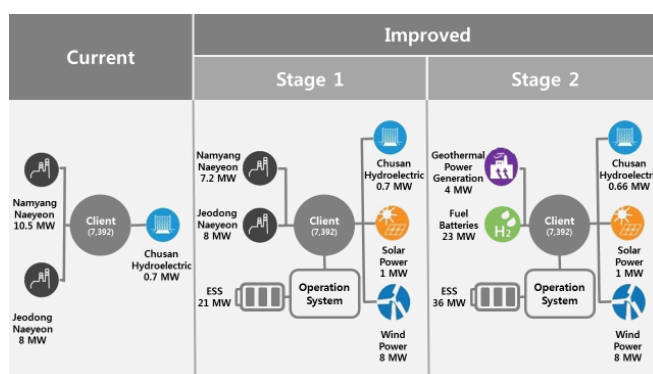


Fig.4. Mix per renewable energy source of the eco-friendly energy independent island project [8]

The Ministry of Trade, Industry and Energy expects that the execution of the first stage itself will reduce the CO<sub>2</sub>emission of Ulleungdo by 4,771 tons and that the completion of the second stage will reduce the CO<sub>2</sub> emission by 13,683 tons.

## V. CONCLUSION

Renewable energy has already contributed to lowering the imported energy dependency substantially and meeting the rapidly growing power demand, yet it is becoming more important to determine the direction of its policy.

Renewable energy, in terms of policy, requires an emphasis in national level. Korea has shown interest and made investments by strengthening national polices. Although its R&D investment per technology has improved the levels of renewable energy, Korea still faces various problems from the viewpoint of activating related industries.

Korea made efforts to realize green growth through various national policies, thus renewable energy sector gradually

management, which 52 islands from thirteen countries joined.

<sup>2</sup> ISLENET is a European islands’ self-governing bodies’ network (ISLENET: European Island Network on Energy & Environment) on sustainable energy supply and environment

through R&D, demonstrations and projects.

In particular, while Korea works toward establishing a powerful government-led national plan, at the same time it also reflects the recommendations of the private working group at its best. Korea has encouraged participation of the private sectors and has promoted market-led measures for commercializing renewable energy.

Thus, breaking away from conventional government-led actions that would simply increase and expand the proportion of the supply of renewable energy sources with regulations and systems, Korea has planned of building eco-friendly energy towns or self-sufficient micro grid projects. Also, it has created a business model that allows participation of private sectors, thereby, the project can be transformed into a market-led one.

In Gasado and Ulleungdo, innovative micro grid systems where ICT and renewable energy sources were converged and compounded were built. In addition, these cases provide good example of changes from a centralized supply system to an independent decentralized power system, creating an environment where potential local renewable energy sources are fully utilized to generate necessary power without an external connection, and in which stable use of energy is possible by building ESS and DR systems.

Although there still exists problems that need to be resolved before commercializing the suggested cases, they are expected to contribute to the global energy market, especially by leading participations from the private sectors among

global energy cooperation.

## References

- [1] Presidential Committee on Green Growth. "National Strategy and five-year Implementation Plan (2009-2013)." Government report, Seoul. 2009
- [2] Basic Act on Low Carbon Green Growth and Related Legislation. 2010
- [3] Presidential Committee on Green Growth. "Commercialization Strategy for Core Green Technologies." Government report, Seoul. 2009
- [4] Green Technology Centre Korea. "National Green Technology R&D Analysis." report, Seoul. 2013
- [5] Ministry of Trade, Industry and Energy. "The Fourth National Master Plan for New and Renewable Energy." Government report, Seoul. September 2014
- [6] Ministry of Trade, Industry and Energy. "The Second National Master Plan for Energy." Government report, Seoul. January 2014
- [7] Ministry of Trade, Industry and Energy. "The Third Development Plan for Energy Technology." Government report, Seoul. December 2014
- [8] Mun Seung-il, "Operational planning of an independent Micogrid", Discussions in the third private/government energy new project conference, 2014.12,  
<http://www.energynewbiz.or.kr/society/working/236?&pageIndex=1>



# Dynamics of surface photo-voltage in GaAs systems studied with time-resolved photoelectron spectroscopy

## 时间分辨光电子能谱下砷化镓系统表面光电压动力学

Masao Kamada<sup>1\*</sup>, Junpei Azuma<sup>1</sup>, Senku Tanaka<sup>2</sup> and Kazutoshi Takahashi<sup>1</sup>

<sup>1</sup>*Synchrotron Light Application Center, Saga University, Saga 840-8502, Japan*

<sup>2</sup>*Department of Electric and Electronic Engineering, Faculty of Science and Engineering, Kinki University, Higashiosaka 577-8502, Japan*

*kamada@cc.saga-u.ac.jp*

Accepted for publication on 15 February 2016

**Abstract** - Experimental data of Surface Photo-Voltage (SPV) on GaAs(100) are presented, which were obtained with time-resolved photoelectron spectroscopy using synchrotron radiation and laser light or ultra-fast laser lights. Clean p- and n-type GaAs with different dopant concentrations were measured at room and low temperatures. The experimental results of the static SPV can be well explained by a thermionic model. On the other hand, the results of the dynamic SPV show clearly the creation and annihilation processes, where the temporal structures of SPV involve slow and fast components. The fast component indicates the important role of hot carriers and non-thermionic process, while the slow one is attributed to the thermionic process. Finally, two ideas for suppressing the SPV effect have been examined to get a higher performance of solar cells and electron emitters.

**Keywords** - Surface Photo-Voltage, Time-resolved photoelectron spectroscopy, Dynamics, GaAs, Non-thermionic process

### I. INTRODUCTION

Solar cells are indispensable devices to generate electric power from natural lights. The key idea originates from a Photo Voltage (PV) effect of semiconductors [1]. Further understandings of the PV mechanism are required to get more efficient, intelligent and cheap solar cells. Moreover, deep understandings of Surface Photo-Voltage (SPV) are required in Schottky-type solar cells and in the field of high-energy accelerator to produce a high-brilliant and ultra-short beam using a photo-cathode [2]. Moreover, the spin electrons attract recent interest for a spin solar cell [3]. These applications need different technologies, internal and external photoelectric effects in semiconductors and interfaces, but the essential point shares common basic understandings. The concepts of band bending and static SPV are based on the electromagnetic theory and a thermionic emission model. In the pn-junction type solar

cells, photo-excited electrons and holes are spatially separated by the internal field caused in the pn junction as well as by the thermal diffusion. Separated electrons and holes produce a reverse electric field. In Schottky-type solar cells, photo-excited electrons and holes are spatially separated by the internal field originated from the interface between metal and semiconductors and also produce a reverse electric field. These reverse electric fields affect the performance of solar cells.

On the other hand, it is essential in the electron sources that photo-excited electrons overcome the surface barrier with the lowest excitation photon energy. The key factors are the large band bending and the low or negative electron affinity. For high brilliant excitation, however, photo-electric yields show saturation or decrease due to the SPV effect: Photo-excited electrons and holes are spatially separated to produce photo currents and a reverse electric field, which affects the performance of electron sources. Therefore, it is important to suppress the SPV effects to improve the efficiency of electron sources as well as solar cells.

Firstly in this report, the present authors introduce their experimental works of SPV on p- and n-type GaAs, which have been obtained with a combinational use of synchrotron radiation (SR) and laser light [4-6]. The differences in static SPV between p- and n-types are explained with a thermionic model. Secondly, dynamics of SPV measured with a time-resolved photoelectron spectroscopy and ultra-fast laser lights are introduced [7-9]. The present results show clearly the creation and annihilation processes of SPV, where temporal structures of SPV involve slow and fast components. The fast component indicates the important role of hot carriers and non-thermionic process, *i.e.* non-equilibrium dynamics, while the slow one is attributed to the thermionic process. Finally, two ideas for suppressing the

SPV effect have been examined in order to get higher performance of solar cells and electron emitters.

## II. EXPERIMENTS

The experiments were carried out at UVSOR BL5A & 6A2 in Institute for Molecular Science and Saga-University BL13 in Saga-LS. Combined systems of SR and laser light with the photoelectron spectroscopy were applied to study SPV effects. As shown in the schematic diagram of the experiments (Fig. 1), sample surfaces were excited with laser light (523 nm or 800 nm) to produce excited electrons and holes. Photoelectrons from a sample core-level were observed using monochromatized SR and hemi-spherical photoelectron spectrometers.

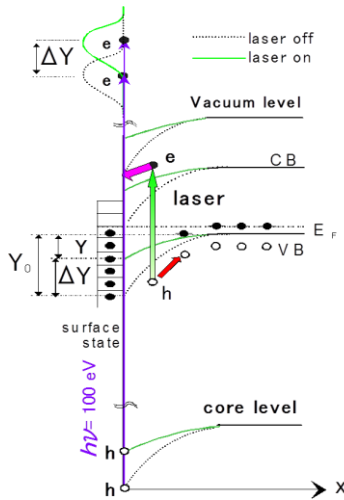


Fig. 1. A schematic diagram of the experiments [5].  $Y_0$ , and  $\Delta Y$  are initial band bending and SPV, respectively. e and h mean an electron and a hole, respectively.

This laser-pump and SR-probe core-level photoelectron spectroscopy has high surface sensitivity, high energy resolution and time resolution (typically, in the subnano to micro second region) besides element-specific and state-selective performances. Moreover, ultra-fast temporal data (typically, in the femto to pico second region) were obtained with a laser-pump and laser-probe photoelectron spectroscopy using Ti:Sapphire femto-second laser systems. The details of the experimental systems have been reported elsewhere [5-6, 10-11], and a typical system is also shown in Fig. 2.

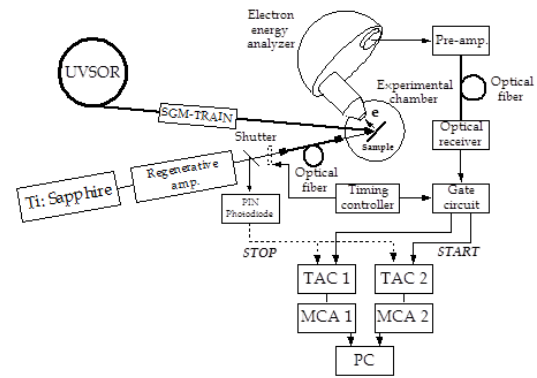


Fig. 2. An experimental system for time-resolved photoelectron spectroscopy [6].

Clean p- and n-type GaAs(100) with different dopant concentrations were measured at room and low temperatures. To investigate the effects of hole mobility, surface barriers and surface states, GaAsP super-lattices and Cr/GaAs(100) samples were investigated [6,12-13]. Surfaces of GaAs were cleaned with a neon-ion sputtering and a thermal annealing, while super-lattice surfaces were cleaned only with thermal treatments. The surface cleanness was checked with an Auger and/or photoelectron spectroscopy after the cleaning procedures, indicating negligible carbon and oxygen contaminations. Moreover, the GaAs (100) surfaces were checked with a low-energy-electron diffraction, showing the  $c(8 \times 2)$  reconstruction.

## III. RESULTS and DISCUSSION

### 3-1. Thermionic model

Semiconductor surfaces show a band bending, which depends on the surface states and dopant concentration. Photoexcited carriers are spatially separated by the internal electric field in the band bending region and by the thermal diffusion. The separated carriers produce SPV as well as photo-currents. In a thermionic model, photo-carriers are assumed to be in the thermal distribution. The dotted curves in Fig. 3 show valence band maximum (VBM) and conduction band minimum (CBM) in the surface region of a p-type semiconductor, which contacts with metallic surface layer, producing a Schottky-type interface. They show the band bending without photoexcitation. The SPV changes the potential in the surface region, which is shown by a solid curve. After approximation procedures in the thermionic model, we can obtain the following Equation (1) [5], where  $p_0$  and  $\delta p$  are initial concentration and increment of positive carriers, respectively, and  $\beta$ ,  $\psi_0$  and  $\Delta\psi$  are  $1/kT$ , initial band bending and SPV, respectively.

$$\ln \{ \beta \Delta \psi \cdot \exp(\beta \Delta \psi) \} \approx \ln \left( \frac{\delta p}{p_0} \right) + \beta \psi_0 \quad (1)$$

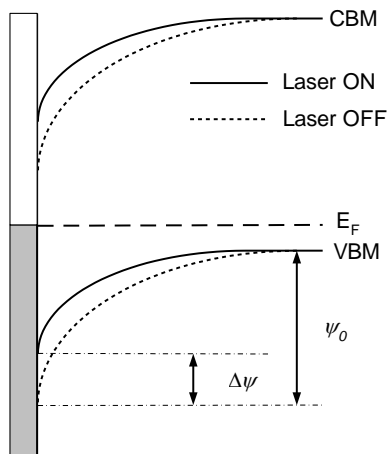


Fig. 3. Band bending and SPV.

3-2. Photon flux dependence of SPV

Figure 4 shows the energy shift of Ga-3d photoelectrons of p-GaAs at 125 K (open circles) as a function of relative incident photon flux. The shift is caused by the SPV under the laser irradiation at 2.33 eV. It is seen that the amount of SPV increases rapidly for low fluxes and gradually increases for middle fluxes, and saturates for higher fluxes. This experimental result is well explained with Eq. (1) mentioned above. Figure 5 shows the comparison of the present result with Eq. (1), where the ordinate and abscissa are presented in natural logarithms according to Eq. (1). The linear solid line and open circles are the theoretical curve and experimental data, respectively. The observed data are in good agreement with the theoretical line from Eq. (1) [5].

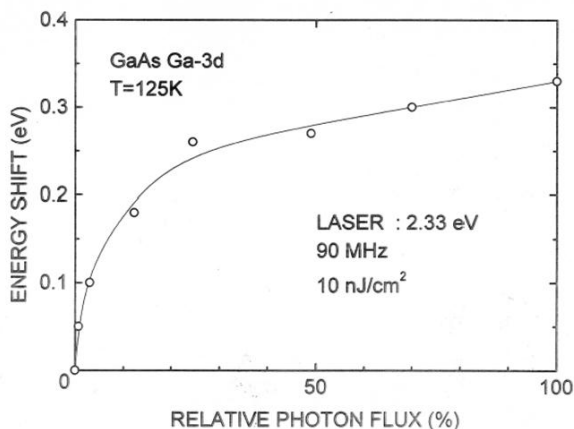


Fig. 4. Energy shift of Ga-3d photoelectrons as a function of incident photon flux.

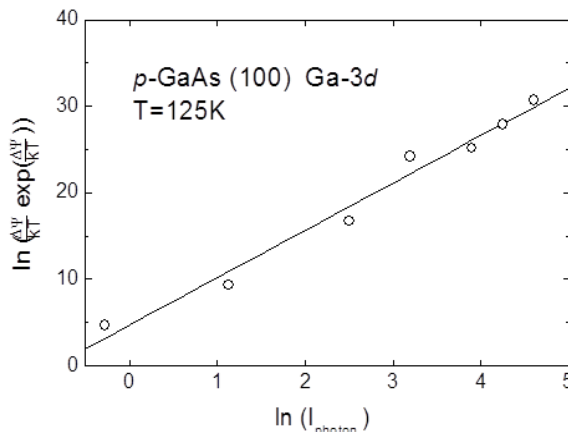


Fig. 5. Comparison of the observed SPV and theoretical line (Eq. (1)) based on a thermionic model [5].

3-3. Temperature dependence of SPV

As Eq. (1) is derived from a thermionic model based on the thermal equilibrium, the temperature dependence of SPV is very important and essential examination for the thermionic

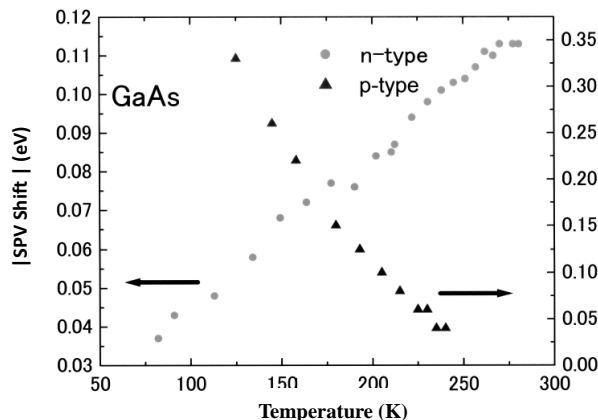


Fig. 6. Temperature dependences of SPV on n-GaAs (solid circle) and p-GaAs (solid triangle). The absolute values are shown for comparison, since the direction of energy shift due to the SPV effect is opposite between p- and n-GaAs.

model. Figure 6 shows the temperature dependences of SPV on p- and n-GaAs (100) surfaces. As the direction of the energy shift of the Ga-3d photoelectrons is opposite between p- and n-GaAs, the absolute values of the energy shift (SPV) are plotted in Fig. 6 as a function of the sample temperature. It is seen that the temperature dependence of SPV is opposite between p- and n-GaAs; *i.e.* the amount of SPV increases in p-GaAs but decreases in n-GaAs as the sample temperature is increased. This difference in the temperature dependence can be explained with the thermionic model as follows. Figure 7 shows the temperature dependence of SPV on p-GaAs, where

the ordinate and abscissa are presented according to Eq. (1) [5].

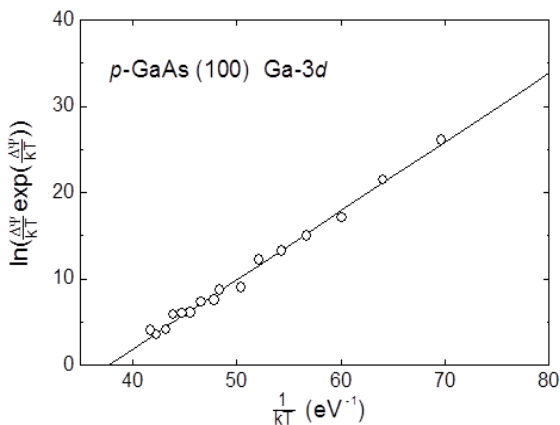


Fig. 7. Temperature dependence of SPV on p-GaAs. The linear line presented according to Eq. (1) fits well the observed data points [5].

The temperature dependence of  $\psi_0$  in Eq. (1) is not clearly described above, but  $\psi_0$  is in general dependent on temperature, since it is determined in the thermal equilibrium between dopant concentration and surface states. The quantity can be observed as the band offset, and the experimental results show that the band bending is

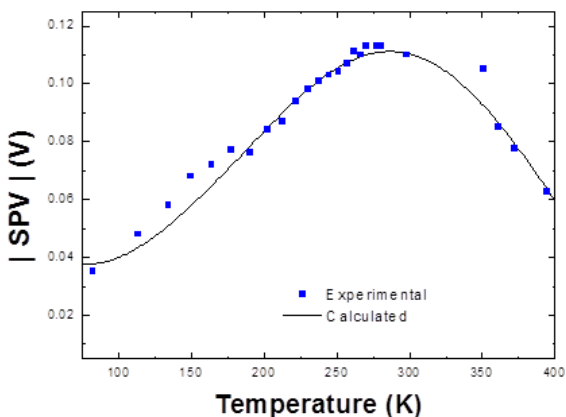


Fig. 8. Temperature dependence of SPV on n-GaAs. The calculated curve includes the temperature dependence of the band bending.

almost temperature independent for p-GaAs, but increases for n-GaAs as the temperature is increased. By taking account of the temperature dependence of  $\psi_0(T)$  and using Eq. (1), the SPV on n-GaAs can be explained, as shown in Fig. 8. Therefore, it is concluded that the temperature dependence of SPV on both p- and n-GaAs is well understood with Eq. (1) based on the thermionic model, and the difference between p- and n-GaAs is attributed mainly to the temperature dependence of the band bending.

### 3-4. Dynamics of SPV

Photoexcited carriers produce photo current and SPV, and the carriers decay to the initial stage. We have carried out the time-resolved experiment to know the dynamics of SPV. The SPV processes are schematically shown in Fig. 9. That is, (a) excited carriers are produced by photo excitation, and subsequently (b) photocarriers are spatially separated to produce photo current and SPV, and (c) the carriers overcome the surface potential barrier and recombine with each other to go back to the initial stage before photoexcitation.

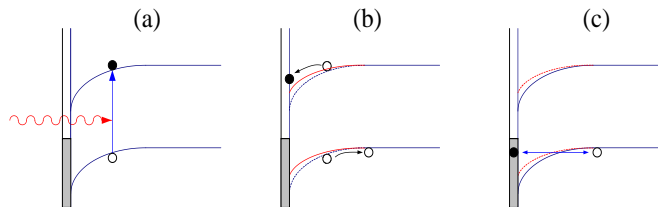


Fig. 9. Three processes of SPV. (a) photoexcitation, (b) creation, and (c) annihilation.

Figure 10 shows the temporal structures of SPV on p-GaAs at room temperature (RT) and 90 K. At RT, the SPV is created and then annihilated in a short period of about  $0.5 \mu s$ , while at 80 K, the SPV decays with a fast component of about  $5 \mu s$  and a slow component accumulated as the background. The slow component is not seen at RT. The present results indicate that a part of SPV is caused by thermal process, while another part is due to non-thermal process [6]. It is supposed that the observed temporal structures are mainly determined by the decay process (c) in Fig. 9.

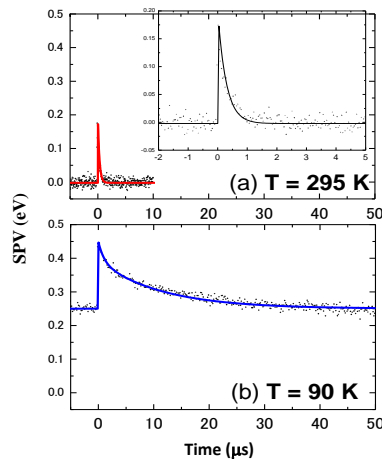


Fig. 10. Temporal structures of SPV at RT and 80 K [6].

### 3-5. Ultra-fast dynamics of SPV

We have measured the ultra-fast time-resolved photoelectron spectra using a laser-pump and laser-probe method. The results show the ultra-fast creation and annihilation processes of SPV. As seen in Fig. 11(a) [8], the

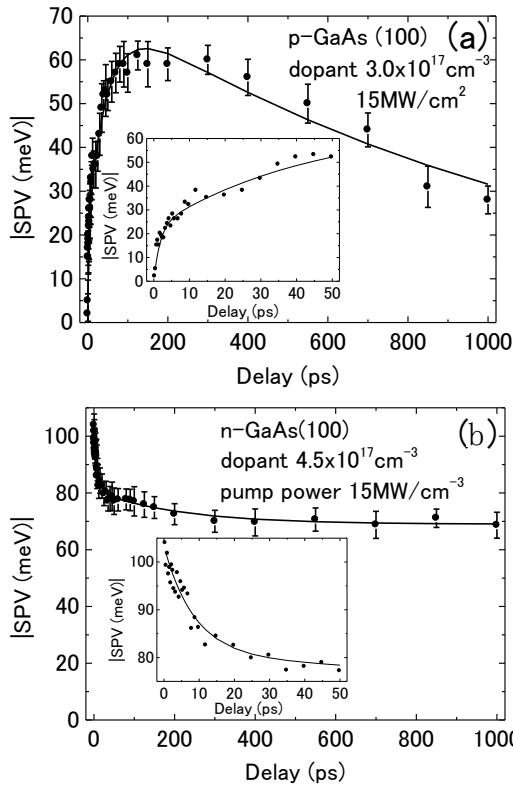


Fig. 11. Ultra-fast temporal structures of SPV. (a) p-GaAs and (b) n-GaAs.

creation process of SPV on p-GaAs has the rise time in pico-second region. The rise time is dependent on dopant concentration: The rise time becomes very fast in case of high dose samples, but it does not clearly show the temperature dependence. On the other hand, the rise process is not observed in Fig. 11(b) for n-GaAs [7], which has the high electron mobility. Therefore, the rise time observed on p-GaAs is attributed to the drift velocity  $v$  which is originated from hole mobility  $\mu$  and inner electric field  $E$  in the band bending region. As seen in Fig. 11(a) and 11(b), the decay time of SPV consists of an ultra-fast and a slow component for both p- and n-GaAs, and the ultra-fast component is independent on the sample temperature, but the slow one has strong temperature dependence and dopant-concentration dependence as well. This result indicates that the decay process of SPV is caused by thermal and non-thermal processes and the ultra-fast component is due to the tunneling process and the slow component is due to the thermionic or thermionic+ tunneling process. Moreover, the total amounts of SPV on n-GaAs depend on excitation density, but the ultra-fast decay component is independent on excitation density. As seen in Fig. 12, the amount and lifetime of the ultra-fast component is almost fixed. (e.g. the lifetime is about 5 ps). Therefore, lifetime of ultra-fast component is due to relaxation time of hot electrons

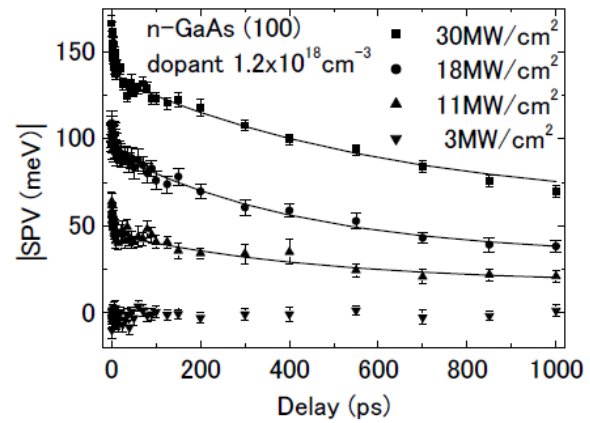


Fig. 12. Excitation density dependence of SPV on n-GaAs in the ultra-fast region.

### 3-6. Two ideas to suppress SPV

High brilliant photon excitation causes the saturation or decrease in solar cells or electron emitters. As mentioned above, one of the main reasons to cause such effects is the SPV, and it is therefore important to suppress SPV in order to have high performance of solar cells or electron emitters. There are two ideas proposed previously [14,15]. One is to control the spatial separation of holes using quantum wells [14]. This is also useful to get high degree of spin polarization for the electron source. Another is to increase recovery force using metallic surface layers [15]. Both ideas were examined by the laser-pump and SR-probe photoelectron spectroscopy and the results were partially

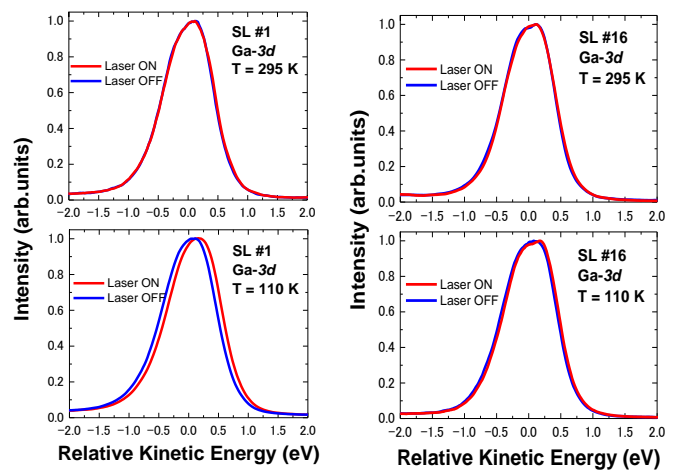


Fig. 13. Ga-3d photoelectron spectra of two super-lattices (SL#1 and SL#16) with and without laser excitations at RT and 110 K.

reported elsewhere [6,13], and the essential points are given in the followings. Figure 13 shows the Ga-3d photoelectron spectra with and without laser excitations on two-types super-lattices (SL#1 and SL#16) at RT and 110K, where the large space charge region of SL#1 and SL#16 is 4 and 34 nm,

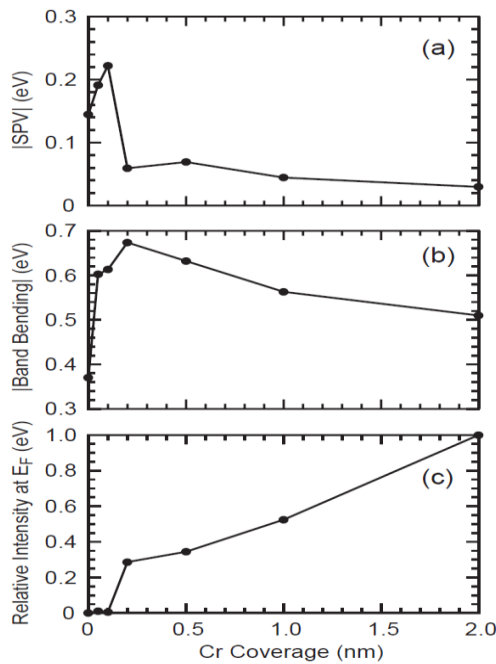


Fig. 14. SPV, band bending, and density of states around Fermi energy of Cr/GaAs as a function of Cr coverage.

respectively. Both spectra observed at RT do not show any SPV and those at 110 K show slight SPV shift. Their temporal structures also indicate negligible SPV at RT and small sharp peak for SL#1, but not for SL#16 [6]. The results mean that the control of the hole transfer in quantum well as well as the thin space charge region are effective to suppress SPV. Figure 14 shows SPV, band bending and density of states around Fermi energy of Cr/GaAs as a function of Cr coverage. The SPV value has a maximum around 0.1 nm of Cr overlayer and decreases as a function of Cr coverage. The decrease of SPV is seemed to relate with the density of states around Fermi energy. It is suggested from the results that the recombination, or quick recovery in the surface region is important to suppress SPV.

### III. SUMMARY

The SPV on p- and n-type GaAs, which have been obtained with a combinational use of synchrotron radiation and laser light, has been reported. The differences in static SPV between p- and n-types are explained with a thermionic model. Dynamic SPV data obtained with a time-resolved photoelectron spectroscopy and ultra-fast laser lights are discussed. The present results show clearly the creation and annihilation processes of SPV, and the temporal structures of SPV consist of slow and fast components. The fast component indicates the important role of hot carriers and non-thermionic process, *i.e.* non-equilibrium dynamics, while the slow one is attributed to the thermionic process. Two ideas for suppressing the SPV effect have been examined in order to get higher performance of solar cells and electron emitters.

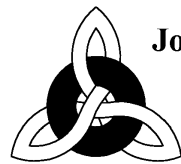
### ACKNOWLEDGEMENTS

The authors express their sincere thanks to Dr. S. Tokudomi and other students in Saga university for their working in this study and in the construction of the experimental setup. This work was partly supported by a Grant-in-Aid for Scientific Research from the Japan Society for the Promotion of Science under grant number (c)25390127.

### REFERENCES

- [1] P. Würfel, *Physics of Solar Cells, From Basic Principles to Advanced Concept*, Weinheim, WILEY-VCH Verlag GmbH&Co. KGaA, 2009.
- [2] K. Hatanaka, T. Nakano, K. Imai and H. Ejiri, *SPIN 2000: 14th International Spin Physics Symposium (AIP Conference Proc.)*, 2000.
- [3] B. Endres, M. Ciorga, M. Schmid, M. Utz, D. Bougeard, D. Weiss, G. Bayreuther and C.H. Back, "Demonstration of the spin solar cell and spin photodiode effect", *Nature Commun.* DOI:10.1038/ncomms 3068, 2013.
- [4] M. Kamada, J. Murakami, S. Tanaka, S. D. More, M. Itoh and Y. Fujii, "Photo-induced change in semiconductor-vacuum interface of p-GaAs(100) studied by photoelectron spectroscopy", *Surface Sci.*, 454-456, pp.525-528, 2000.
- [5] S. Tanaka, S. D. More, J. Murakami, M. Itoh, Y. Fujii and M. Kamada, "Surface photovoltage effects on p-GaAs(100) from core-level photoelectron spectroscopy using synchrotron radiation and a laser", *Phys. Rev. B* 64, pp.155308-1-155308-6, 2001.
- [6] S. Tanaka, T. Nishitani, T. Nakanishi, S. D. More, J. Azuma, K. Takahashi, O. Watanabe and M. Kamada, "Surface photovoltage effect and its time dependence in GaAs-GaAsP superlattice studied with combination of synchrotron and laser radiation" *J. Appl. Physics* 95, pp.551-556, 2004.
- [7] S. Tokudomi, J. Azuma, K. Takahashi and M. Kamada, "Ultrafast Decay of Surface Photo-Voltage Effect on n-type GaAs (100) Surface", *J. Phys. Soc. Jpn.* 76, pp.104710-1-104710-4, 2007.
- [8] S. Tokudomi, J. Azuma, K. Takahashi and M. Kamada, "Ultrafast Time Dependence of Surface Photo-Voltage Effect on p-type GaAs(100) Surface" *J. Phys. Soc. Jpn.* 77, pp.014711-1-014711-5, 2008.
- [9] J. Azuma, K. Takahashi and M. Kamada, "Direct observation of the dispersion and relaxation of photoexcited electrons in InAs", *Phys. Rev. B* 81, pp.113203-1-113203-4, 2010.
- [10] K. Takahashi, Y. Kondo, J. Azuma and M. Kamada, "Beamline for high-resolution angle-resolved photoemission at Saga Light Source", *J. Elect. Spectr. & Related Phenom.*, 144/147, pp.1093-1096, 2005.
- [11] K. Takahashi, J. Azuma, S. Tokudomi and M. Kamada, "Development of the Experimental System for Time- and Angle-resolved Photoemission Spectroscopy", *AIP Conf. Proc.* (9th Int. Conf. SRI) 879, pp.1218-1221, 2007.
- [12] S. Tanaka, S.D. More, T. Nishitani, K. Takahashi, T. Nakanishi and M. Kamada, "Surface-photovoltage effect on GaAs-GaAsP super-lattice studied with combination of synchrotron radiation and laser" *Surface Rev. and Lett.* 9, pp.1297-1301, 2002.
- [13] K. Takahashi, S. Tokudomi, Y. Nagata, J. Azuma and M. Kamada, "Surface Photo-Voltage Effect on Cr/GaAs(100) Studied by Photoemission Spectroscopy with the Combination of Synchrotron Radiation and Laser" *J. Appl. Phys.* 110, pp.113711, 2011.

- [14] T. Nakanishi, "Workshop report on spin polarized electron source and polarimeter", *AIP conf. Proc.*, 570, pp.274-285, 2001.
- [15] A. Herrera-Gómez, G. Vergara and W. E. Spicer, "Physics of high - intensity nanosecond electron source: Charge limit phenomenon in GaAs photocathodes", *J. Appl. Phys.* 79, pp.7318-7323, 1996.



**Journal of Energy Challenges  
and Mechanics**

ISSN 2056-9386

<http://www.nscj.co.uk/JECM/>

**Editor:**

Dr. Henry Tan  
University of Aberdeen, Scotland, United Kingdom

**Scope:**

Since James Watt, a Scottish inventor, improved efficiency of the steam engine, human civilization relies more and more on a steady supply of energy. Today we are at a transitional age. On the one hand, we see technology advances in the exploration and development of oil and gas, a depleting resource; we see growth in handling aging and decommissioning. On the other hand, we see ideas and plans for new energy infrastructure. This journal is about energy challenges and the underlying mechanics, involving multiple disciplines in science, technology, management and policy-making. Mechanics, fundamentally, is about force and the related behaviours, where force is about relationships, including those physical, human and social. For mechanics, the journal covers interactive boundaries with many other disciplines. For energy, topics include both fossil fuels and many different forms of renewable energy; also, issues related to energy economy, energy policy, efficiency, safety, environment and ecology will also be covered.



Cove Bay, Aberdeen, Scotland, United Kingdom